iScience

CellPress

Article

Oxygen Defects in β-MnO_2 Enabling High-Performance Rechargeable Aqueous Zinc/Manganese Dioxide Battery

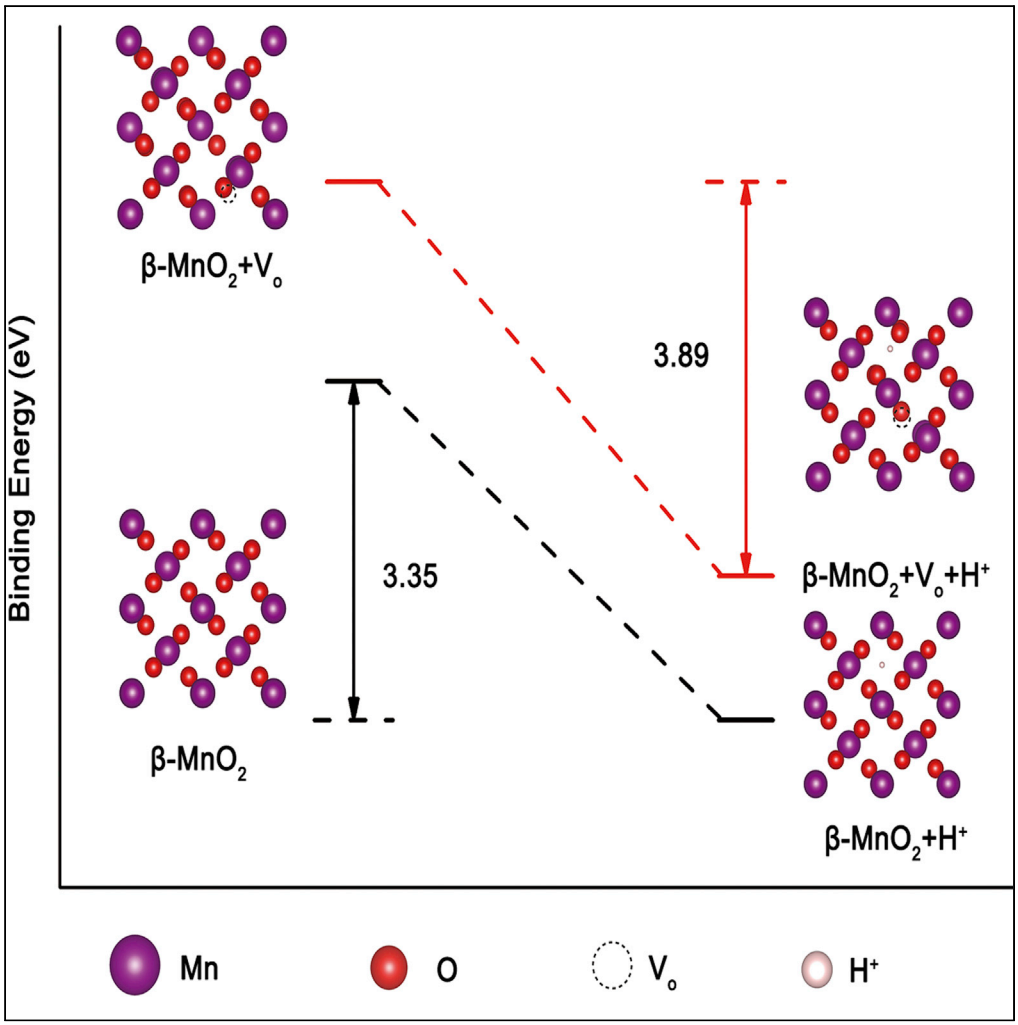

Mingming Han, Jiwu Huang, Shuquan Liang, ..., Yiren Wang, Shan Guo, Jiang Zhou

lsq@csu.edu.cn (S.L.)
yiren.wang@csu.edu.cn (Y.W.)
zhou_jiang@csu.edu.cn (J.Z.)

HIGHLIGHTS

A conversion reaction mechanism is observed for Zn/β-MnO_2 system

The binding energy of H^+ insertion is reduced by introducing oxygen defects

The introduction of oxygen defects increases ion insertion channels

Zn/D-β-MnO_2 battery delivers good performance even at high mass loading

Han et al., iScience *23*, 100797 January 24, 2020
https://doi.org/10.1016/j.isci.2019.100797

iScience

CellPress

Article

Oxygen Defects in β-MnO_2 Enabling High-Performance Rechargeable Aqueous Zinc/Manganese Dioxide Battery

Mingming Han,[1] Jiwu Huang,[1] Shuquan Liang,[1,2,*] Lutong Shan,[1] Xuesong Xie,[1] Zhenyu Yi,[1] Yiren Wang,[1,*] Shan Guo,[1] and Jiang Zhou[1,2,3,*]

SUMMARY

Rechargeable aqueous Zn/manganese dioxide (Zn/MnO_2) batteries are attractive energy storage technology owing to their merits of low cost, high safety, and environmental friendliness. However, the β-MnO_2 cathode is still plagued by the sluggish ion insertion kinetics due to the relatively narrow tunneled pathway. Furthermore, the energy storage mechanism is under debate as well. Here, β-MnO_2 cathode with enhanced ion insertion kinetics is introduced by the efficient oxygen defect engineering strategy. Density functional theory computations show that the β-MnO_2 host structure is more likely for H^+ insertion rather than Zn^{2+}, and the introduction of oxygen defects will facilitate the insertion of H^+ into β-MnO_2. This theoretical conjecture is confirmed by the capacity of 302 mA h g^{-1} and capacity retention of 94% after 300 cycles in the assembled aqueous Zn/β-MnO_2 cell. These results highlight the potentials of defect engineering as a strategy of improving the electrochemical performance of β-MnO_2 in aqueous rechargeable batteries.

INTRODUCTION

Among the various electrochemical energy storage devices, lithium-ion batteries have dominated the commercial rechargeable battery market because of their high energy density and excellent cycling stability (Wang et al., 2019a; Yin et al., 2018; Zhou et al., 2018a). However, the high cost of lithium source and the safety issue associated with flammable organic electrolyte limited their applications in large-scale energy storage systems (Fang et al., 2018a; Tan et al., 2019; Wang et al., 2019b). In this regard, there is urgent demand for alternative advanced rechargeable battery technologies. Aqueous rechargeable metal-ion batteries have become promising choice because of their high safety, low cost, and high ionic conductivity compared with the organic cells (Kundu et al., 2016; Wang et al., 2012). Some aqueous rechargeable batteries based on the insertion/extraction of Na^+ (Liu et al., 2014; Bin et al., 2018), K^+ (Su et al., 2016), Mg^{2+} (Chen et al., 2017), Al^{3+} (Liu et al., 2012), and Zn^{2+} (Dai et al., 2018; Xu et al., 2012; Li et al., 2018; Zhang et al., 2015a) have already been investigated. Rechargeable aqueous zinc-ion batteries (ZIBs) have particularly attracted much attention because of the abundance of Zn and some impressive attributes of Zn anode that include high theoretical specific capacity (819 mA h g^{-1}) and low redox potential (−0.76 V versus standard hydrogen electrode) (Fang et al., 2018b; Liu et al., 2019a; Song et al., 2018; Wan et al., 2018; Yang et al., 2018; Zhang et al., 2016a).

MnO_2 has been a promising cathode material since the primary alkaline Zn/MnO_2 batteries were introduced in the 1860s due to its abundance, cost-effectiveness, and eco-friendliness (Xu et al., 2012; Zhang et al., 2016a; Minakshi et al., 2004; Biswal et al., 2015; Sundaram et al., 2016). However, the formation of unwanted irreversible by-products like $Mn(OH)_2$ or Mn_2O_3 on the cathode side and $Zn(OH)_2$ or ZnO on anode side leads to poor coulombic efficiency and severe capacity fading in the alkaline Zn/MnO_2 systems (Boden et al., 1967; McBreen, 1975; Hertzberg et al., 2016). In an attempt to improve the performance of Zn/MnO_2 cells, mild acidic $ZnSO_4$-based electrolyte has recently been used, and the strategy resulted in great improvement (Xu et al., 2012; Zhang et al., 2019; Zhao et al., 2018). Up to now, various types of MnO_2 (like α-MnO_2, γ-MnO_2 or δ-MnO_2, etc.) with different polymorphs have displayed satisfactory electrochemical performances in ZIBs due to their appreciable tunneled or layered structure (Alfaruqi et al., 2015a, 2015b; Huang et al., 2018a; Ko et al., 2018; Sun et al., 2017), and their polyhedral representations are shown in Figures S1A–S1C. β-MnO_2, a technologically important material for energy storage, has already been widely used in lithium-ion batteries and supercapacitors (Jiao and Bruce, 2007; Zhu et al., 2018). However,

[1]School of Materials Science and Engineering, Central South University, Changsha 410083, China

[2]Key Laboratory of Electronic Packaging and Advanced Functional Materials of Hunan Province, Central South University, Changsha 410083, China

[3]Lead Contact

*Correspondence: lsq@csu.edu.cn (S.L.), yiren.wang@csu.edu.cn (Y.W.), zhou_jiang@csu.edu.cn (J.Z.)

https://doi.org/10.1016/j.isci.2019.100797

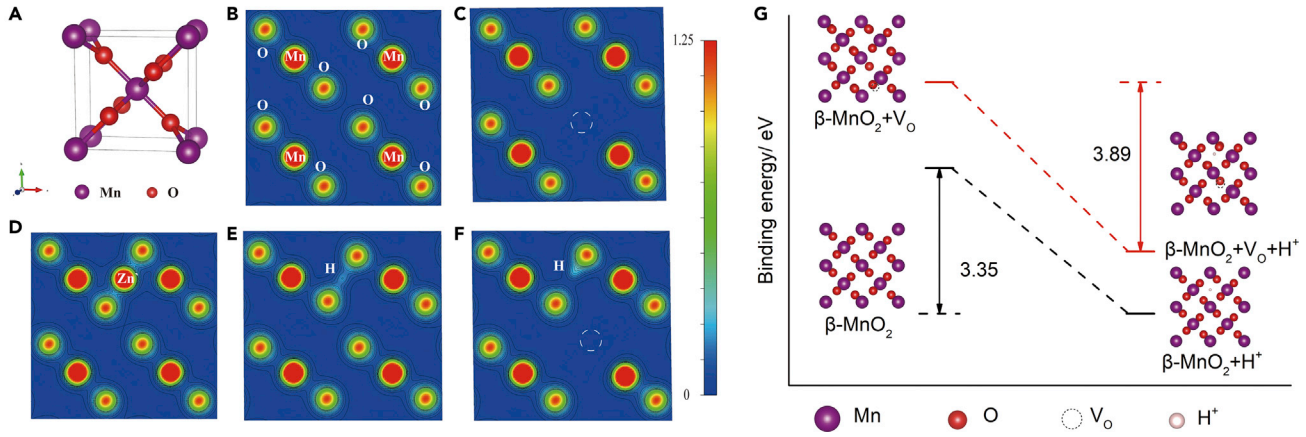

Figure 1. DFT Calculations for H^+ and Zn^{2+} Insertion into β-MnO_2

(A) The pristine β-MnO_2 bulk structure; (B-F) Charge density distribution in the units of electrons/Å^3 for supercell with different concerned defects in the (001) plane: (B) Pristine β-MnO_2 supercell; (C) β-MnO_2 supercell contains a V_O; (D) β-MnO_2 supercell inserted a Zn^{2+} ion; (E) β-MnO_2 inserted a H^+ ion; (F) β-MnO_2 supercell contains a V_O and inserted a H^+ ion, the dashed spheres indicate the vacancy sites; (G) Calculated H^+ insertion energy barriers for β-MnO_2 with or without V_O.

its narrow tunnel size and the strong electrostatic interaction between β-MnO_2 host cathode and guest ions result in sluggish ion insertion kinetics (Wang et al., 2018; Islam et al., 2017). Although modifying MnO_2 with different polymorphs, hybridizing with conducting materials, or enlarging the interlayer spacing seems an available approach to improve the electrochemical performances (Huang et al., 2018b; Vatsalarani et al., 2005), defects engineering can be considered as another approach for enhancing the electrochemical performance of Zn/β-MnO_2 batteries. Defect engineering could imbue the metal oxide with some unusual physicochemical properties (Dawson et al., 2015; Liu et al., 2019b; Zeng et al., 2018). Among the various defect types, oxygen vacancy (V_O) is one kind of effective technique for modifying surface chemistry (Liu et al., 2019b; Zhao et al., 2019). First, V_O enables the charge and ion transport process by changing the electronic structure, resulting in improved ion insertion kinetics. Second, V_O facilitates phase transition by modifying the thermodynamics on the electrode surface (Zhang et al., 2016b; Zou et al., 2019).

Another debate on MnO_2 cathode is the energy storage mechanism (Li et al., 2019). The most prominent energy release or storage mechanism involves Zn^{2+} insertion or extraction into or from the host materials during the electrochemical process (Alfaruqi et al., 2015b; Zhang et al., 2017). However, some cases demonstrate a Zn^{2+} and H^+ co-insertion process (Sun et al., 2017), conversion reaction mechanism (Pan et al., 2016), combination displacement/intercalation reaction (Shan et al., 2019a), or Zn-driven reduction displacement reaction (Shan et al., 2019b). Different insertion thermodynamics and kinetics of H^+ and Zn^{2+} would contribute to the different reaction mechanisms, which results from the various polymorphs, particle sizes of the positive electrode, or electrolyte systems (Xiong et al., 2019). Remarkably, we proved the different kinetics of Zn^{2+} and H^+ insertion into β-MnO_2 through density functional theory (DFT) calculations and experimental measurements. The results indicate that the energy required for H^+ to insert into and react with the nearest-neighboring O atoms in perfect β-MnO_2 is about 1.63 eV lower than that of Zn^{2+} owing to the large ionic radius of Zn^{2+} (Figures 1A–1F). Moreover, the binding energy of H^+ insertion into β-MnO_2 would be further reduced and a conversion reaction process would be speeded up by introducing oxygen defects (Figures 1G and S2).

Herein, we report a zinc/manganese dioxide aqueous system using β-MnO_2 with rich oxygen defects (noted as D-β-MnO_2) in $ZnSO_4$-based electrolyte. A conversion reaction mechanism between H^+ and MnO_2 is observed for the Zn/β-MnO_2 aqueous system by experimental and DFT calculation results. The D-β-MnO_2 cathode displayed a discharge capacity of 302 mA h g^{-1} at 50 mA g^{-1}, a capacity retention of 94% after 300 cycles at 500 mA g^{-1}, which is higher than 206 mA h g^{-1} and 78% retention for the commercial β-MnO_2. Furthermore, the D-β-MnO_2 electrode with a mass loading of 3.0 mg cm^{-2} showed a maximum discharge capacity of 268 mA h g^{-1} at 50 mA g^{-1}, and even at a high current density of 1,000 mA g^{-1}, it still delivered a capacity of 112 mA h g^{-1}. Interestingly, the electrode still displayed a high discharge capacity of 163 mA h g^{-1} even at a higher mass loading of 4.0 mg cm^{-2} of the active material.

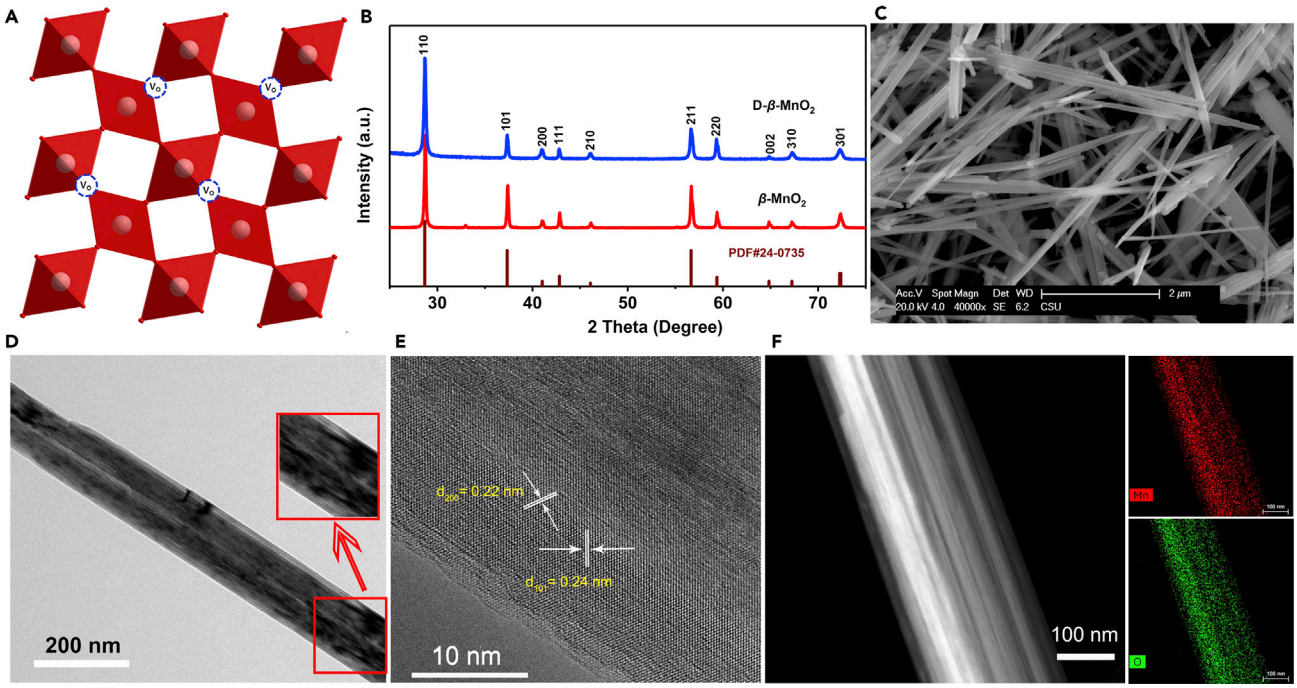

Figure 2. Microstructure Characterization of D-β-MnO_2

(A) Crystal structure of rutile-type D-β-MnO_2; (B) XRD patterns of commercial β-MnO_2 and D-β-MnO_2; (C) SEM, (D) TEM, (E) HR-TEM, and (F) EDX mapping images of Mn and O elements of D-β-MnO_2 sample.

The performance may be not much better than those of previously reported Zn/MnO_2 cells (Xiong et al., 2019; Zhang et al., 2017), but the presented results enlighten the potential application of oxygen-defected β-MnO_2 cathode in aqueous rechargeable batteries.

RESULTS AND DISCUSSION

Structure Identification and Characterization of β-MnO_2

Oxygen defects were introduced into β-MnO_2 through a successive calcination and reduction treatment; the detailed synthesis process is shown in Transparent Methods (Supplemental Information). Crystal structure analysis (Figure 2A) reveals that the D-β-MnO_2 compound possesses a tunneled structure interlinked with the basic structure unit of [MnO_{6-x}] octahedron by sharing corners. X-ray diffraction (XRD) patterns demonstrate that the as-prepared sample possesses similar crystalline phase as commercial β-MnO_2 (Figure 2B). The characteristic peaks suggest a high-purity property of the prepared tetragonal phase (JCPDS: 24-0735) with P42/mnm space group, which is expressed in Figure S3. Both the scanning electron microscopic (SEM) and transmission electron microscopic (TEM) images (Figures 2C and 2D) confirm that the D-β-MnO_2 sample possesses one-dimensional homogeneous nanorod morphology. The nanorods are several micrometers in length and about 100 nm in width. The lattice distance of 0.24 nm corresponds to the (101) crystal plane of β-MnO_2 in high-resolution transmission electron microscopy (HR-TEM) image (Figure 2E). Moreover, energy-dispersive X-ray (EDX) elemental mapping images in Figure 2F suggest the homogeneous distribution of Mn and O elements in D-β-MnO_2.

To gain insights into the structural differences between commercial β-MnO_2 and D-β-MnO_2, TEM and HR-TEM were carried out. As displayed in Figures 3A and 3B, the commercial β-MnO_2 shows clear lattice fringes with lattice spacing of 0.31 nm assigned to (110) plane of perfect β-MnO_2, indicating that the commercial β-MnO_2 possesses nearly defect-free crystal structure. However, the D-β-MnO_2 sample exhibits a rough surface with various small pits, which may be created by the oxygen defects (Figures 2D and 3C). (Zhang et al., 2016b) Besides the pits (marked by the arrows in Figure 3C), slight lattice disorder and dislocations can also be observed at different sections in D-β-MnO_2 (Figures 3C and S4). Moreover, blurred sections in the HR-TEM image and the weak intensities of some continuous distributed Mn and O atoms marked by boxes in Figure 3D further confirm the rich defects in D-β-MnO_2 (Chen et al., 2019; Yao et al.,

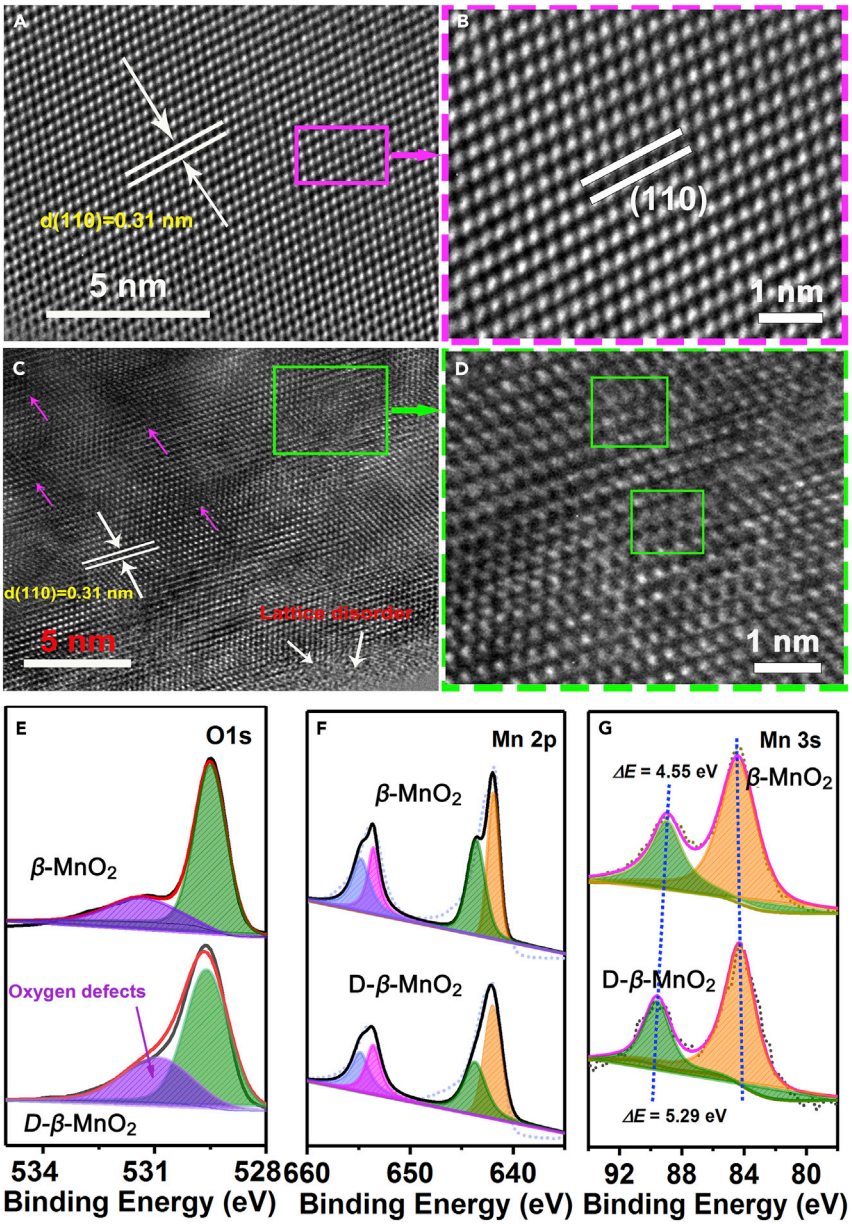

Figure 3. Structure and Valence Analysis of β-MnO_2

(A–D) HR-TEM images of (A and C) commercial β-MnO_2 and D-β-MnO_2 samples, respectively, and (B and D) images of the areas as marked in (A and C), respectively.

(E–G) High-resolution (E) O 1s, (F) Mn 2p, and (G) Mn 3s XPS spectra for commercial β-MnO_2 and D-β-MnO_2 samples.

2019). In addition, the oxygen defects were further verified by the X-ray photoelectron spectroscopy (XPS) measurement and Raman spectra. As shown in Figure 3E, the peak at 529.5 eV for both samples is attributed to the lattice oxygen ubiquitously in oxide semiconductors. The peak centered at 531.2 eV is assigned to oxygen species beside the oxygen vacancies (Li and Su, 2019). The higher intensity and larger integrated area in D-β-MnO_2 than that in commercial β-MnO_2 confirm the existence of rich oxygen defects in D-β-MnO_2. It is also confirmed by the Mn 2p XPS spectra (Figure 3F), which showed stronger intensity of Mn^{3+} in D-β-MnO_2 than that in commercial β-MnO_2. Previous reports have clarified the linear relationship between the energy separation of Mn 3s peaks and the valence of Mn in oxides (Lei et al., 2016). The energy separation of 5.29 eV in D-β-MnO_2 is wider than that (4.55 eV) of commercial β-MnO_2 (Figure 3G), suggesting a lower average valence of Mn in D-β-MnO_2 (Cheng et al., 2013), which may be caused by the oxygen

deficiency. The Raman spectra of the two samples showed a Mn-O vibration peak centered at 649 cm^{-1} (Xia et al., 2017). However, compared with the commercial β-MnO_2 sample, there is a reduction of the intensity of the Mn-O vibration peak in D-β-MnO_2, indicating a decreased content of Mn-O bond caused by the oxygen defects (Figure S5). Also, the composition of D-β-MnO_2 was analyzed by EDX, and the result indicates that the compositional ratio of Mn and O is 1:1.75. Herein, we define the amount of "Mn" as "1" and use it to calibrate the content of "O." Therefore, the D-β-MnO_2 could be expressed as $MnO_{1.75}$ and the content of oxygen defects is about 12.5%, which is similar with that (11.2%) calculated according to the XPS result (Figures 3F and S6).

Application for Zn-Ion Battery and Electrochemical Performance of β-MnO_2

To investigate the effects of oxygen defects on the electrochemical performances, CR2016 (the diameter of the positive shell is 20 mm and the height is 1.6 mm) cells were assembled using β-MnO_2 cathode, Zn foil anode, $ZnSO_4$-based aqueous electrolyte, and glass fiber separator. The cyclic voltammetry (CV) curves tested at 0.2 mV s^{-1} are shown in Figures 4A and S7. The almost overlapped profiles after the gradual activation of the two initial cycles indicate good reversibility of the cell (Figure S7). Moreover, the polarization potentials (0.21 V, 0.31 V) of D-β-MnO_2 electrode are lower than those (0.23 V, 0.40 V) of commercial β-MnO_2 at the first (1.61/1.40) and second (1.56/1.25) redox pairs (Figure 4A). In addition, CV curves at 0.1 and 0.3 mV s^{-1} were tested (Figure S8), which showed similar profiles, and both the CV curves showed higher peak current response and smaller polarization potential of D-β-MnO_2 electrode than that of commercial β-MnO_2 electrode, demonstrating a higher reaction activity of D-β-MnO_2. The discharge capacity can be observed through galvanostatic charge/discharge (GCD) profiles shown in Figure 4B. It shows a high discharge capacity of 302 mA h g^{-1} of D-β-MnO_2, which is much higher than that of commercial β-MnO_2.

The enhanced performance of D-β-MnO_2 could be attributed to the introduction of oxygen defects, which increased ion absorption sites and opened up extra ion insertion channels, resulting in higher reaction activity and higher capacity (Fang et al., 2019). Nevertheless, the delivered capacity of D-β-MnO_2 electrode in this work was a bit lower than that reported by Minakshi's work (Minakshi, 2008), which may be due to the different crystal structures or energy storage mechanisms in the two distinct systems, but it surpassed that of some reported cathode materials, which can be seen in Table S1. Furthermore, the energy and power densities also surpassed those of many reported materials, like $ZnMn_{1.86}O_4$ (Zhang et al., 2016a), $NaV_3O_8 \cdot 1.5H_2O$ (Wan et al., 2018), $V_2O_5 \cdot nH_2O$/rGO (Yan et al., 2018), $LixV_2O_5 \cdot nH_2O$ (Yang et al., 2018), and so on, as shown in the Ragone plot (Figure 4C). In addition, the Zn/D-β-MnO_2 battery was also assembled by using porous Zn anode instead of Zn foil to study the effect of porosity on the discharge capacity (Minakshi and Ionescu, 2010; Minakshi et al., 2010). The result, however, did not show significant improvement in discharge capacity (Figure S9).

The positive effects of oxygen defects on cyclability have already been proved in LIBs and sodium-ion batteries (Yao et al., 2018). However, the relevant researches on ZIBs are seldom reported. As shown in Figure 4D, commercial β-MnO_2 electrode delivers a discharge capacity of 182 mA h g^{-1} after 50 cycles at 100 mA g^{-1}. In contrast, there is still a high discharge capacity of 276 mA h g^{-1} for the Zn/D-β-MnO_2 cell. Furthermore, the Zn/D-β-MnO_2 battery delivers high capacity retention of 94% at 500 mA g^{-1} after 300 cycles, which is higher than that (78%) of commercial β-MnO_2-based cells (Figure 4F). In addition, the positive effect of the introduction of oxygen defects is also reflected by the improved electrical conductivity, as shown by electrochemical impedance spectroscopy (EIS, Figure S10 and Table S2). It shows a smaller charge-transfer resistance (R_{ct}, 257 Ω at the initial state, 46 Ω after 10 cycles) of the D-β-MnO_2 electrode compared with commercial MnO_2 electrode (R_{ct}, 610 Ω at the initial state, 178 Ω after 10 cycles), manifesting enhanced electrical conductivity after the introduction of oxygen defects (Barmi and Minakshi, 2016).

As for the promising large-scale energy storage devices, the rechargeable Zn/MnO_2 batteries not only need to provide high energy density and long cycling stability with a low active material loading but also need to ameliorate the cell-fabrication parameters to reach a stable electrochemical performance with a sufficient amount of MnO_2 active material. Therefore, the Zn/D-β-MnO_2 batteries were tested with active material loadings of about 3.0 and 4.0 mg cm^{-2}, respectively. Figure 4E shows the rate performances of the battery with the D-β-MnO_2 loading about 3.0 mg cm^{-2}. It is interesting to observe that the maximum discharge capacity of 268 mA h g^{-1} can be achieved at 50 mA g^{-1}, even though the current density increased to 1,000 mA g^{-1}, the battery could still deliver a capacity of 112 mA h g^{-1}. Furthermore, the

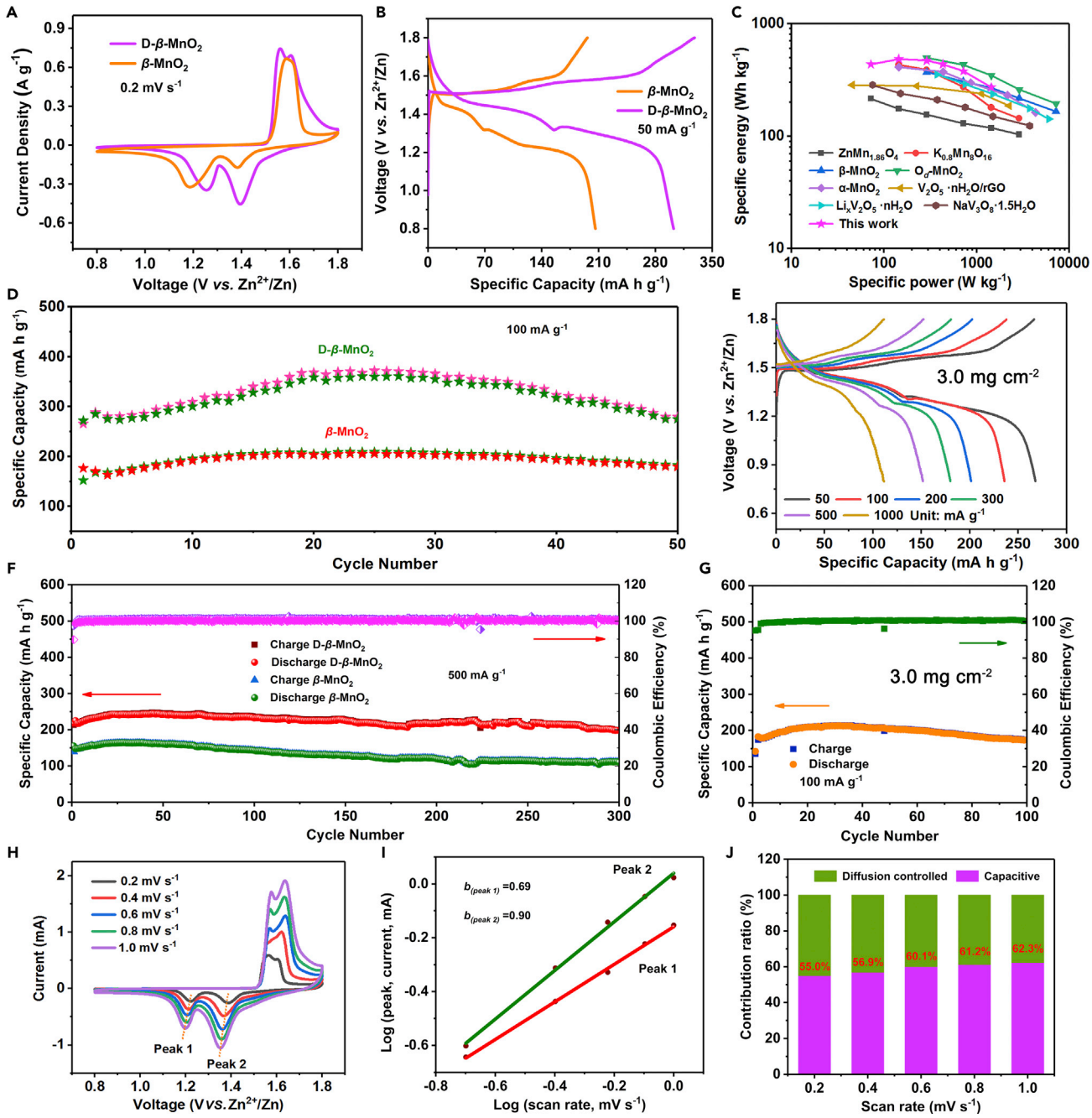

Figure 4. Electrochemical Performance Comparisons between Commercial β-MnO_2 and D-β-MnO_2 Electrodes

(A-F) (A) CV curves at 0.2 mV s^{-1}; (B) GCD profiles at 50 mA g^{-1}; (C) Ragone plot of Zn/D-β-MnO_2 cell, comparing with other reported cathode materials; (D and F) Cycling performances at 100 and 500 mA g^{-1}. (E and G) (E) GCD curves at different current densities and (G) cycling performance at 100 mA g^{-1} of the D-β-MnO_2 electrodes with a mass loading of 3.0 mg cm^{-2}. (H-J) (H) CV curves at different scan rates, (I) the corresponding plots of log (peak current) *vs.* log (scan rate) at the redox peaks and (J) the calculated capacitive contributions at different scan rates of D-β-MnO_2 electrodes.

Zn/D-β-MnO_2 batteries show high capacity retention of 82% compared with the maximum discharge capacity after 100 cycles at 100 mA g^{-1} (Figure 4G). Similarly, the batteries still display a discharge capacity of 163 mA h g^{-1} with a higher active material loading of 4.0 mg cm^{-2} (Figures S11A and S11B). It is to be noted that the electrodes with high mass loading exhibit almost the same open circuit voltage as the electrode at low mass loading. However, they showed an increased polarization potential of 0.27 V for

D-β-MnO_2 electrode at a mass loading of 3.0 mg cm^{-2} and 0.30 V for the D-β-MnO_2 electrode at 4.0 mg cm^{-2} in the initial cycle (Figure S12), which are higher than that of D-β-MnO_2 electrode (0.22 V) at a mass loading of 1.3 mg cm^{-2}. The increased polarization potentials may be due to the increased charge transfer and ion diffusion resistance. In addition, the commercial β-MnO_2 electrodes at mass loadings of 3.0 and 4.0 mg cm^{-2} were also tested, and relatively lower discharge capacity was observed (Figures S13A–S13D).

As discussed before, DFT calculations have revealed that the introduction of oxygen defects would reduce the energy barrier for H^+ insertion. To confirm the fast rate of H^+ ion insertion kinetics in D-β-MnO_2 (H^+ is the main charge carrier in this work, which will be discussed in following section), the CV curves of the D-β-MnO_2 sample were tested from 0.2 to 1.0 mV s^{-1} (Figure 4H). The relationship between the CV current and the scan rate obey the power law ($i = av^b$, where i refers to current, v refers to the scan rate, and a and b are adjustable parameters) (Yan et al., 2018). In general, the b value is in the range of 0.5–1.0 (He et al., 2017). As for the D-β-MnO_2 sample, the b-value calculated by the slopes of the redox peaks of peak 1 and peak 2, are 0.69 and 0.90, respectively (Figure 4I), demonstrating a favored capacitive kinetics in D-β-MnO_2 sample (Yao et al., 2019). In addition, the capacitive contributions of the above-mentioned different electrochemical processes can be calculated by the equation $i = k_1v + k_2v^{1/2}$, where i refers to current response, k_1v represents capacitive contribution, and $k_2v^{1/2}$ represents ion-diffusion contribution. As a result, at 0.2 mV s^{-1}, 55% of the capacity is determined to be capacitive for D-β-MnO_2. With the increase of scan rates, the percentage of capacitive contribution increases to 56.9%, 60.1%, 61.2%, and 62.3% at scan rates of 0.4, 0.6, 0.8, and 1.0 mV s^{-1}, respectively, indicating that the capacitive contribution holds the main position in the total capacity.

Galvanostatic intermittent titration technique was adopted to investigate the diffusion coefficients of H^+ in β-MnO_2 electrodes because the diffusion coefficient is another parameter to evaluate the reaction kinetics (Figure S14). (Fang et al., 2019) The calculated diffusion coefficient value (1.35×10^{-11} cm^2 S^{-1}) of D-β-MnO_2 electrode at second discharge plateaus is much higher than that (1.73×10^{-12} cm^2 S^{-1}) of commercial β-MnO_2 electrode, which is even higher than that of Li^+ in β-MnO_2 electrode (Wang et al., 2016). It further proved that the introduction of oxygen defects would improve the ion insertion kinetics. The reason for the fast H^+ insertion kinetics during the charge/discharge process could be explained by Figure 5A (the H^+ diffusion along [001] direction in ab plane). As shown in the diagram, the abundant oxygen defects opened up the [MnO_6] polyhedron walls, resulting in extra ion channels in the distorted [MnO_6] units, which would be beneficial for the insertion of guest ions into the electrode (Fang et al., 2019).

Reaction Mechanism of Aqueous Zn/β-MnO_2 Cell

An understanding of the prevailing electrochemical reaction mechanism of a cell is important. Here, *ex situ* tests like Fourier transform infrared (FTIR) spectroscopy, XRD, XPS, and TEM were carried out to study the structural evolutions of D-β-MnO_2 during the electrochemical process. The selected states in the first and second cycles were marked in Figure 5B. It is interesting to discover that the strong XRD diffraction peaks (Figure 5C) corresponding to $Zn_4SO_4(OH)_6\cdot xH_2O$ in the discharge process dominate the XRD patterns of other phases, such as, β-MnO_2 and MnOOH. Subsequently, these signals disappear after charging to 1.8 V. Apart from the XRD, FTIR spectroscopy is another powerful technique to characterize the materials. The FTIR spectra (Figure 5D) were obtained in the range from 400 to 2,000 cm^{-1}; they are marked by the labels A–L corresponding to Figure 5B. The absorption peaks at 600 and 1,120 cm^{-1} during the discharge process are ascribed to Zn-O bond and SO_4^{2-} in $Zn_4SO_4(OH)_6\cdot xH_2O$ (Wan et al., 2018). However, the intensity of the two peaks weakened and completely disappeared at the fully charged state. The XRD and FTIR results collaboratively demonstrate the reversible formation and disappearance of $Zn_4SO_4(OH)_6\cdot xH_2O$ in the electrochemical process. Moreover, SEM images were used to further investigate the structure evolutions (Figure S15). Flake-like solids were observed clearly in the fully discharged stage, which may be the $Zn_4SO_4(OH)_6\cdot xH_2O$ compounds. They disappeared later, and an interconnected porous layer is observed after charging. It is to be noted that the commercial β-MnO_2 electrode undergoes the same reaction behavior and structural evolutions during the discharge and charge processes (Figures S16 and S17).

In the Zn/D-β-MnO_2 cells, the water solvent in electrolytically decomposed into OH^- and H^+, with a large amount of OH^- ions reacting with $ZnSO_4$ forming $Zn_4SO_4(OH)_6\cdot xH_2O$. To reach a neutral charge system, the H^+ ions move into the host structure and react with MnO_2 electrode, forming MnOOH during the discharge process (Pan et al., 2016). In addition, the reversible formation and disappearance of

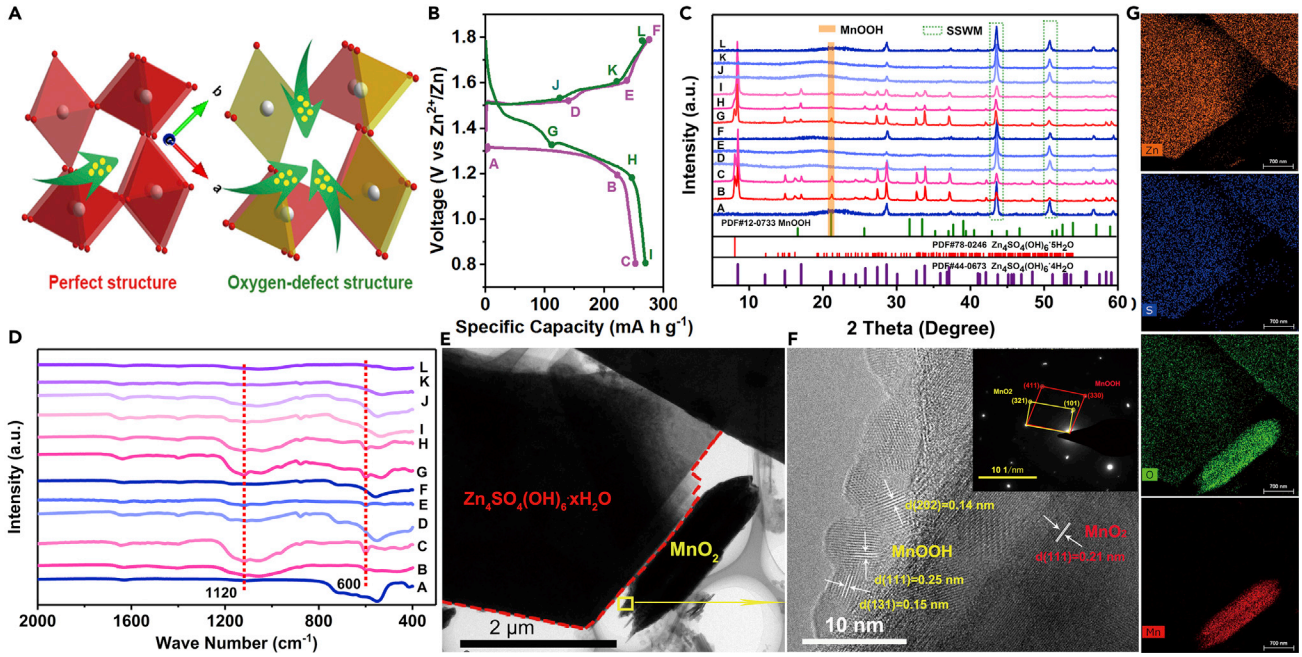

Figure 5. H^+ Ions Diffusion Paths in β-MnO_2 and Structure Evolution of D-β-MnO_2

(A) Schematic illustration of H^+ ion diffusion paths in β-MnO_2 with perfect and oxygen defect structure; (B) GCD curves at 50 mA g^{-1} for the initial two cycles; (C and D) The corresponding *ex situ* (C) XRD patterns and (D) FTIR spectra at selected states; (E–G) (E) TEM image, (F) HR-TEM image, with inset showing the corresponding SAED pattern, and (G) the corresponding EDX elemental mappings of the electrode at the fully discharged state.

$Zn_4SO_4(OH)_6 \cdot xH_2O$ and MnOOH also demonstrates the good reversibility of this Zn/β-MnO_2 system. It can also be supported by the XRD pattern of the MnO_2 cathode after 50 cycles (Figure S18), which revealed the same peaks with the pristine electrode. To further prove the H^+ insertion mechanism, high-resolution XPS of O 1s and Mn 2p at different states and ^1H nuclear magnetic resonance (NMR) study were conducted (Figures 6 and S19). The high-resolution XPS spectra of O element (Figures 6A–6C) indicate that there are almost no -OH (532.8 eV) and Mn-O-H (531.5 eV) (Jabeen et al., 2016; Zhang et al., 2015b) signals in the initial state. However, the two signals appeared at discharged state accompanied by decreased intensities at charged state. It is to be noted that the –OH signal may come from the $Zn_4SO_4(OH)_6 \cdot xH_2O$, and the Mn-O-H signal, from MnOOH. The Mn 2p XPS spectra shows increased contents of Mn^{3+} and Mn^{2+} at the fully discharged state compared with the initial state. Reversibly, they decreased after charging to 1.8 V. Furthermore, the ^1H NMR study also confirms the formation of $Zn_4SO_4(OH)_6 \cdot xH_2O$ and the change of magnetic susceptibility of the electrode at the discharged state. All the results confirmed that the $Zn_4SO_4(OH)_6 \cdot xH_2O$ and MnOOH formed in discharged state and decomposed in charged state, which is consistent with the XRD and FTIR results.

As suggested by the above-mentioned results, the energy storage mechanism involves H^+ insertion, but whether or not Zn^{2+} ions have participated in the energy storage process was studied by TEM images at the fully discharged state. Figure 5E presents a kind of flake-like solid that is $Zn_4SO_4(OH)_6 \cdot xH_2O$ compound, as supported by EDX mappings (Figure 5G), which reveals intense signals of Zn and S. However, the Mn and O elements are mainly distributed on the nanorod. This observation supports the fact that Zn^{2+} ions have not participated in the energy storage process. Moreover, HR-TEM images (Figure 5F) of the nanorod exhibit two kinds of lattice fringes, which match well with MnO_2 and MnOOH phases. The corresponding selected area electron diffraction (SAED) patterns also confirm the formation of MnOOH on the surface of MnO_2 electrode.

In addition, the conversion reaction mechanism was proved by assembling the Zn/D-β-MnO_2 cell using organic electrolyte containing Zn^{2+}. The limited discharge capacity further indicates that the energy storage in this Zn/D-β-MnO_2 system is from the conversion reaction between H^+ and MnO_2 (note: Zn can reversibly strip/plate in this organic electrolyte as reported in other literature, Pan et al., 2016; Figure S20).

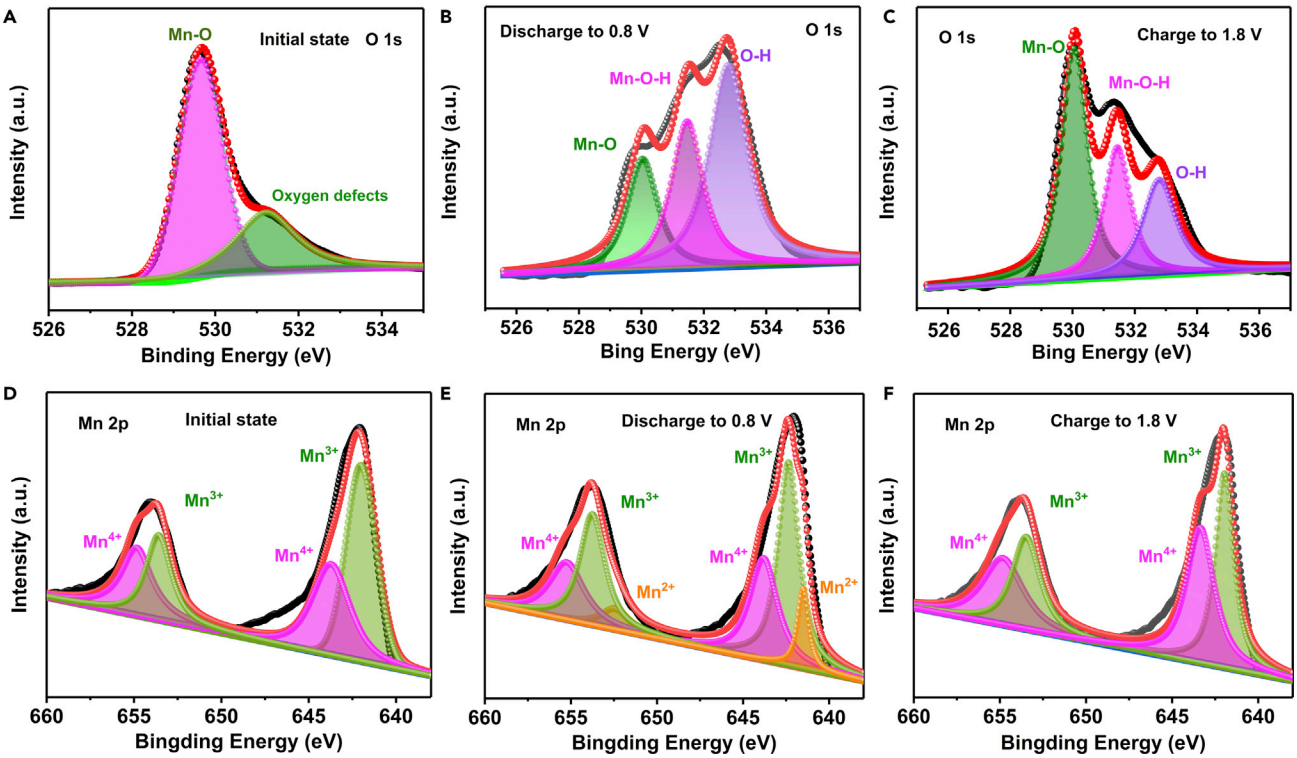

Figure 6. High-Resolution O 1s and Mn 2p XPS Spectra for D-β-MnO_2

Electrodes at different states: (A-C) The O 1s XPS spectra at initial, discharged and charged states in the second cycle, respectively; (D-F) The Mn 2p XPS spectra at initial, discharged and charged states in the second cycle, respectively.

All the aforementioned results indicate a conversion mechanism in this Zn/MnO_2 cell, and the electrochemical reaction equation is listed in the Supplemental Information, which is similar to the literature reported by Liu's group (Pan et al., 2016). However, the limitation of our experimental condition may make it hard to unveil the veil of the energy storage mechanism deeply. More experimental data or advanced characterization techniques would be needed to understand the reaction mechanism in the future.

Conclusion

In summary, we have investigated the Zn/β-MnO_2 aqueous battery chemistry, in terms of its energy storage mechanism and the performance improvement strategy by introducing oxygen defects. The introduction of abundant oxygen defects into the β-MnO_2 reduces the binding energy of H^+ insertion into β-MnO_2. In addition, the energy storage mechanism is demonstrated as a conversion reaction process between H^+ and MnO_2. It is interesting to find that the D-β-MnO_2 electrode displays a discharge capacity of 302 mA h g^{-1} at 50 mA g^{-1} and 114 mA h g^{-1} even at 2,000 mA g^{-1} and a capacity retention of 94% after 300 cycles at 500 mA g^{-1}. Such Zn/D-β-MnO_2 cells will pave way for advanced large-scale energy storage applications.

Limitations of the Study

The effects of oxygen vacancy were confirmed by electrochemical results, DFT, TEM, and XPS in this work. However, to further get the insight of the effects of oxygen vacancy, *in situ* characterization is still needed but is very challenging. In addition, the limitation of our experimental condition may make it hard to unveil the veil of the energy storage mechanism deeply. More experimental data or advanced characterization techniques would be needed to understand the reaction mechanism in the future.

METHODS

All methods can be found in the accompanying Transparent Methods supplemental file.

SUPPLEMENTAL INFORMATION

Supplemental Information can be found online at https://doi.org/10.1016/j.isci.2019.100797.

ACKNOWLEDGMENTS

This work was supported by National Natural Science Foundation of China (Grant nos. 51932011, 51972346, 51802356, and 51872334) and Innovation-Driven Project of Central South University (No. 2018CX004)

AUTHOR CONTRIBUTIONS

J.Z. and M.H. designed the project. M.H. wrote the manuscript. The experiments were carried out by M.H. and Z.Y. Y.W. carried out the DFT calculations. S.G. provided helpful suggestions on the DFT calculations. X.X., J.H., and S.L. helped to polish the manuscript. All the authors discussed the results and commented on the manuscript.

DECLARATION OF INTERESTS

The authors declare no competing interests.

Received: July 22, 2019
Revised: September 29, 2019
Accepted: December 18, 2019
Published: January 24, 2020

REFERENCES

Alfaruqi, M.H., Gim, J., Kim, S., Song, J., Pham, D.T., Jo, J., Xiu, Z., Mathew, V., and Kim, J. (2015a). A layered δ-MnO_2 nanoflake cathode with high zinc-storage capacities for eco-friendly battery applications. Electrochem. Commun. *60*, 121–125.

Alfaruqi, M.H., Mathew, V., Gim, J., Kim, S., Song, J., Baboo, J.P., Choi, S.H., and Kim, J. (2015b). Electrochemically induced structural transformation in a γ-MnO_2 cathode of a high capacity zinc-ion battery system. Chem. Mater. *27*, 3609–3620.

Barmi, M.J., and Minakshi, M. (2016). Tuning the redox properties of the nanostructured $CoMoO_4$ electrode: effects of surfactant content and synthesis temperature. ChemPlusChem. *81*, 964–977.

Bin, D., Wang, F., Tamirat, A.G., Suo, L., Wang, Y., Wang, C., and Xia, Y. (2018). Progress in aqueous rechargeable sodium-ion batteries. Adv. Energy Mater. *8*, 1703008.

Biswal, A., Tripathy, B.C., Sanjay, K., Subbaiah, T., and Minakshi, M. (2015). Electrolytic manganese dioxide (EMD): a perspective on worldwide production, reserves and its role in electrochemistry. RSC Adv. *5*, 58255–58283.

Boden, D., Venuto, C.J., Wisler, D., and Wylie, R.B. (1967). The alkaline manganese dioxide electrode I. The discharge process. J. Electrochem. Soc. *114*, 415–417.

Chen, L., Bao, J.L., Dong, X., Truhlar, D.G., Wang, Y., Wang, C., and Xia, Y. (2017). Aqueous Mg-ion battery based on polyimide anode and Prussian blue cathode. ACS Energy Lett. *2*, 1115–1121.

Chen, S., Wang, H., Kang, Z., Jin, S., Zhang, X., Zheng, X., Qi, Z., Zhu, J., Pan, B., and Xie, Y. (2019). Oxygen vacancy associated single-electron transfer for photofixation of CO_2 to long-chain chemicals. Nat.Commun. *10*, 788.

Cheng, F., Zhang, T., Zhang, Y., Du, J., Han, X., and Chen, J. (2013). Enhancing electrocatalytic oxygen reduction on MnO_2 with vacancies. Angew. Chem. Int. Ed. *52*, 2474–2477.

Dai, X., Wan, F., Zhang, L., Cao, H., and Niu, Z. (2018). Freestanding graphene/VO_2 composite films for highly stable aqueous Zn-ion batteries with superior rate performance. Energy Storage Mater. *17*, 143–150.

Dawson, J.A., Chen, H., and Tanaka, I. (2015). First-principles calculations of oxygen vacancy formation and metallic behavior at a beta-MnO_2 grain boundary. ACS Appl. Mater. Interfaces *7*, 1726–1734.

Fang, G., Wu, Z., Zhou, J., Zhu, C., Cao, X., Lin, T., Chen, Y., Wang, C., Pan, A., and Liang, S. (2018a). Observation of pseudocapacitive effect and fast ion diffusion in bimetallic sulfides as an advanced sodium-ion battery anode. Adv. Energy Mater. *8*, 1703155.

Fang, G., Zhou, J., Pan, A., and Liang, S. (2018b). Recent advances in aqueous zinc-ion batteries. ACS Energy Lett. *3*, 2480–2501.

Fang, G., Zhu, C., Chen, M., Zhou, J., Tang, B., Cao, X., Zheng, X., Pan, A., and Liang, S. (2019). Suppressing manganese dissolution in potassium manganate with rich oxygen defects engaged high-energy-density and durable aqueous zinc-ion battery. Adv. Funct. Mater. *29*, 1808375.

He, P., Quan, Y., Xu, X., Yan, M., Yang, W., An, Q., He, L., and Mai, L. (2017). High-performance aqueous zinc-ion battery based on layered $H_2V_3O_8$ nanowire cathode. Small *13*, 1702551.

Hertzberg, B.J., Huang, A., Hsieh, A., Chamoun, M., Davies, G., Seo, J.K., Zhong, Z., Croft, M., Erdonmez, C., Meng, Y.S., and Steingart, D. (2016). Effect of multiple cation electrolyte mixtures on rechargeable Zn–MnO_2 alkaline battery. Chem. Mater. *28*, 4536–4545.

Huang, J., Wang, Z., Hou, M., Dong, X., Liu, Y., Wang, Y., and Xia, Y. (2018a). Polyaniline-intercalated manganese dioxide nanolayers as a high-performance cathode material for an aqueous zinc-ion battery. Nat. Commun. *9*, 2906–2913.

Huang, Y., He, W., Zhang, P., and Lu, X. (2018b). Nitrogen-doped MnO_2 nanorods as cathodes for high-energy Zn-MnO_2 batteries. Funct. Mater. Lett. *11*, 1840006.

Islam, S., Alfaruqi, M.H., Mathew, V., Song, J., Kim, S., Kim, S., Jo, J., Baboo, J.P., Pham, D.T., Putro, D.Y., et al. (2017). Facile synthesis and the exploration of the zinc storage mechanism of β-MnO_2 nanorods with exposed (101) planes as a novel cathode material for high performance eco-friendly zinc-ion batteries. J. Mater. Chem. A *5*, 23299–23309.

Jabeen, N., Xia, Q., Savilov, S.V., Aldoshin, S.M., Yu, Y., and Xia, H. (2016). Enhanced pseudocapacitive performance of α-MnO_2 by cation preinsertion. ACS Appl. Mater. Interfaces *8*, 33732–33740.

Jiao, F., and Bruce, P.G. (2007). Mesoporous crystalline β-MnO_2—a reversible positive electrode for rechargeable lithium batteries. Adv. Mater. *19*, 657–660.

Ko, J.S., Sassin, M.B., Parker, J.F., Rolison, D.R., and Long, J.W. (2018). Combining battery-like and pseudocapacitive charge storage in 3D MnO_x@carbon electrode architectures for zinc-ion cells. Sustain. Energy Fuels *2*, 626–636.

Kundu, D., Adams, B.D., Duffort, V., Vajargah, S.H., and Nazar, L.N. (2016). A high-capacity and

long-life aqueous rechargeable zinc battery using a metal oxide intercalation cathode. Nat. Energy *1*, 16119.

Lei, K., Cong, L., Fu, X., Cheng, F., and Chen, J. (2016). Stirring-assisted hydrothermal synthesis of ultralong α-MnO_2 nanowires for oxygen reduction reaction. Inorg. Chem. Front. *3*, 928–933.

Li, S.S., and Su, Y.K. (2019). Improvement of the performance in Cr-doped ZnO memory devices via control of oxygen defects. RSC Adv. *9*, 2941–2947.

Li, H., Han, C., Huang, Y., Huang, Y., Zhu, M., Pei, Z., Xue, Q., Wang, Z., Liu, Z., Tang, Z., et al. (2018). An extremely safe and wearable solid-state zinc ion battery based on a hierarchical structured polymer electrolyte. Energy Environ. Sci. *11*, 941–951.

Li, Y., Wang, S., Salvador, J.R., Wu, J., Liu, B., Yang, W., Yang, J., Zhang, W., Liu, J., and Yang, J. (2019). Reaction mechanisms for long-life rechargeable Zn/MnO_2 batteries. Chem. Mater. *31*, 2036–2047.

Liu, S., Hu, J.J., Yan, N.F., Pan, G.L., Li, G.R., and Gao, X.P. (2012). Aluminum storage behavior of anatase TiO_2 nanotube arrays in aqueous solution for aluminum ion batteries. Energy. Environ. Sci. *5*, 9743–9746.

Liu, Y., Qiao, Y., Zhang, W., Xu, H., Li, Z., Shen, Y., Yuan, L., Hu, X., Dai, X., and Huang, Y. (2014). High-performance aqueous sodium-ion batteries with $K_{0.27}MnO_2$ cathode and their sodium storage mechanism. Nano Energy *5*, 97–104.

Liu, F., Chen, Z., Fang, G., Wang, Z., Cai, Y., Tang, B., Zhou, J., and Liang, S. (2019a). V_2O_5 nanospheres with mixed vanadium valences as high electrochemically active aqueous zinc-ion battery cathode. Nano Micro Lett. *11*, 25–36.

Liu, G., Li, J., Fu, J., Jiang, G., Lui, G., Luo, D., Deng, Y.P., Zhang, J., Cano, Z.P., Yu, A., et al. (2019b). An Oxygen-vacancy-rich semiconductor-supported bifunctional catalyst for efficient and stable zinc-air batteries. Adv. Mater. *31*, 1806761.

McBreen, J. (1975). The electrochemistry of β-MnO_2 and γ-MnO_2 in alkaline electrolyte. Electrochim. Acta *20*, 221–225.

Minakshi, M. (2008). Examining manganese dioxide electrode in KOH electrolyte using TEM technique. J. Electroanal.Chem. *616*, 99–106.

Minakshi, M., and Ionescu, M. (2010). Anodic behavior of zinc in Zn-MnO_2 battery using ERDA technique. Int. J. Hydrogen Energy *35*, 7618–7622.

Minakshi, M., Singh, P., Issa, T.B., Thurgate, S., and Marco, D.R. (2004). Lithium insertion into manganese dioxide electrode in MnO_2/Zn aqueous battery: Part II. Comparison of the behavior of EMD and battery grade MnO2 in Zn|MnO2| aqueous LiOH electrolyte. J. Power Sources *138*, 319–322.

Minakshi, M., Appadoo, D., and Martin, D.E. (2010). The anodic behavior of planar and porous zinc electrodes in alkaline electrolye. Electrochem. Solid State Lett. *13*, A77–A80.

Pan, H., Shao, Y., Yan, P., Cheng, Y., Han, K.S., Nie, Z., Wang, C., Yang, J., Li, X., Bhattacharya, P., et al. (2016). Reversible aqueous zinc/manganese oxide energy storage from conversion reactions. Nat. Energy *1*, 16039.

Shan, L., Yang, Y., Zhang, W., Chen, H., Fang, G., Zhou, J., and Liang, S. (2019a). Observation of combination displacement/intercalation reaction in aqueous Zinc-ion battery. Energy Storage Mater. *18*, 10–14.

Shan, L., Zhou, J., Han, M., Fang, G., Cao, X., Wu, X., and Liang, S. (2019b). Reversible Zn-driven reduction displacement reaction in aqueous Zinc-ion battery. J. Mater. Chem. A *7*, 7355–7359.

Song, M., Tan, H., Chao, D., and Fan, H.J. (2018). Recent advances in Zn-ion batteries. Adv. Funct. Mater. *28*, 1802564.

Su, D., McDonagh, A., Qiao, S.Z., and Wang, G. (2016). High capacity aqueous potassium ion batteries for large scale energy storage. Adv. Mater. *29*, 1604007.

Sun, W., Wang, F., Hou, S., Yang, C., Fan, X., Ma, Z., Gao, T., Han, F., Hu, R., Zhu, M., and Wang, C. (2017). Zn/MnO_2 battery chemistry with H^+ and Zn^{2+} coinsertion. J. Am. Chem. Soc. *139*, 9775–9778.

Sundaram, M.M., Biswal, A., Mitchell, D., Jones, R., and Fernandez, C. (2016). Correlation among physical and electrochemical behaviour of nanostructured electrolytic manganese dioxide from leach liquor and synthetic for aqueous asymmetric capacitor. Phys. Chem. Chem. Phys. *18*, 4711–4720.

Tan, H., Chen, D., Rui, X., and Yu, Y. (2019). Peering into alloy anodes for sodium-ion batteries: current trends, challenges, and opportunities. Adv. Funct. Mater. *29*, 1808745.

Vatsalarani, J., Trivedi, D.C., Ragavendran, K., and Warrier, P.C. (2005). Effect of polyaniline coating on "shape change" phenomenon of porous zinc electrode. J. Electrochem. Soc. *152*, 1974–1978.

Wan, F., Zhang, L., Dai, X., Wang, X., Niu, Z., and Chen, J. (2018). Aqueous rechargeable zinc/sodium vanadate batteries with enhanced performance from simultaneous insertion of dual carriers. Nat. Commun. *9*, 1656–1666.

Wang, Y., Yi, J., and Xia, Y. (2012). Recent progress in aqueous lithium-ion batteries. Adv. Energy Mater. *2*, 830–840.

Wang, M., Yang, Q., Zhang, T., Zhu, B., and Li, G. (2016). Facile synthesis of β-MnO_2/polypyrrole nanorods and their enhanced lithium-storage properties. RSC Adv. *6*, 19952–19956.

Wang, F., Hu, E., Sun, W., Gao, T., Ji, X., Fan, X., Han, F., Yang, X.Q., Xu, K., and Wang, C. (2018). A rechargeable aqueous Zn^{2+}-battery with high power density and a long cycle-life. Energy Environ. Sci. *11*, 3168–3175.

Wang, B., Ryu, J., Choi, S., Zhang, X., Pribat, D., Li, X., Zhi, L., Park, S., and Ruoff, R.S. (2019a). Ultrafast-charging silicon-based coral-like network anodes for lithium-ion batteries with high energy and power densities. ACS Nano *13*, 2307–2315.

Wang, J., Fan, L., Liu, Z., Chen, S., Zhang, Q., Wang, L., Yang, H., Yu, X., and Lu, B. (2019b). In situ alloying strategy for exceptional potassium ion batteries. ACS Nano *13*, 3703–3713.

Xia, L., Pan, L., Asif, M., Zhang, D., Usman, M., Yang, S., Zhou, N., Hu, Y., and Bin, Y. (2017). Facile fabrication of polyaniline@γ-MnOOH on a buckypaper ternary composite electrode for free-standing supercapacitors. RSC Adv. *7*, 44523–44530.

Xiong, T., Yu, Z.G., Wu, H., Du, Y., Xie, Q., Chen, J., Zhang, Y.-W., Pennycook, S.J., Lee, W.S.V., and Xue, J. (2019). Defect engineering of oxygen-deficient manganese oxide to achieve high-performing aqueous zinc ion battery. Adv. Energy Mater. *9*, 1803815.

Xu, C., Li, B., Du, H., and Kang, F. (2012). Energetic zinc ion chemistry: The rechargeable zinc ion battery. Angew. Chem. Int. Ed. *51*, 933–935.

Yan, M., He, P., Chen, Y., Wang, S., Wei, Q., Zhao, K., Xu, X., An, Q., Shuang, Y., Shao, Y., et al. (2018). Water-lubricated intercalation in V_2O_5 nH_2O for high-capacity and high-rate aqueous rechargeable zinc batteries. Adv. Mater. *30*, 1703725.

Yang, Y., Tang, Y., Fang, G., Shan, L., Guo, J., Zhang, W., Wang, C., Wang, L., Zhou, J., and Liang, S. (2018). Li^+ intercalated $V_2O_5 \cdot nH_2O$ with enlarged layer spacing and fast ion diffusion as an aqueous zinc-ion battery cathode. Energy Environ. Sci. *11*, 3157–3162.

Yao, X., Ke, Y., Ren, W., Wang, X., Xiong, F., Yang, W., Qin, M., Li, Q., and Mai, L. (2018). Defect-rich soft carbon porous nanosheets for fast and high-capacity sodium-ion storage. Adv. Energy Mater. *9*, 1803260.

Yao, K., Xu, Z., Huang, J., Ma, M., Fu, L., Shen, X., Li, J., and Fu, M. (2019). Bundled defect-rich MoS_2 for a high-rate and long-life sodium-ion battery: achieving 3D diffusion of sodium ion by vacancies to improve kinetics. Small *15*, 1805405.

Yin, B., Cao, X., Pan, A., Luo, Z., Dinesh, S., Lin, J., Tang, Y., Liang, S., and Cao, G. (2018). Encapsulation of CoSx nanocrystals into N/S Co-doped honeycomb-like 3D porous carbon for high-performance lithium storage. Adv. Sci. *5*, 1800829.

Zeng, Y., Lai, Z., Han, Y., Zhang, H., Xie, S., and Lu, X. (2018). Oxygen-vacancy and surface modulation of ultrathin nickel cobaltite nanosheets as a high-energy cathode for advanced zn-ion batteries. Adv. Mater. *30*, 1802396.

Zhang, L., Chen, L., Zhou, X., and Liu, Z. (2015a). Morphology-dependent electrochemical performance of zinc hexacyanoferrate cathode for zinc-ion battery. Sci. Rep. *5*, 18263.

Zhang, T., Cheng, F., Du, J., Hu, Y., and Chen, J. (2015b). Efficiently enhancing oxygen reduction electrocatalytic activity of MnO_2 using facile hydrogenation. Adv. Energy Mater. *5*, 1400654.

Zhang, N., Cheng, F., Liu, Y., Zhao, Q., Lei, K., Chen, C., Liu, X., and Chen, J. (2016a). Cation-deficient spinel $ZnMn_2O_4$ cathode in $Zn(CF_3SO_3)_2$ electrolyte for rechargeable aqueous Zn-ion battery. J. Am. Chem. Soc. *138*, 12894–12901.

Zhang, N., Li, X., Ye, H., Chen, S., Ju, H., Liu, D., Lin, Y., Ye, W., Wang, C., Xu, Q., et al. (2016b). Oxide defect engineering enables to couple solar energy into oxygen activation. J. Am. Chem. Soc. *138*, 8928–8935.

Zhang, N., Cheng, F., Liu, J., Wang, L., Long, X., Liu, X., Li, F., and Chen, J. (2017). Rechargeable aqueous zinc-manganese dioxide batteries with high energy and power densities. Nat. Commun. *8*, 405–413.

Zhang, L., Rodríguez-Pérez, I.A., Jiang, H., Zhang, C., Leonard, D.P., Guo, Q., Wang, W., Han, S., Wang, L., and Ji, X. (2019). $ZnCl_2$ "water-in-salt" electrolyte transforms the performance of vanadium oxide as a Zn battery cathode. Adv. Funct. Mater. *29*, 1902653.

Zhao, Q., Huang, W., Luo, Z., Liu, L., Lu, Y., Li, Y., Hu, J., Ma, H., and Chen, J. (2018). High-capacity aqueous zinc batteries using sustainable quinone electrodes. Sci. Adv. *4*, eaao1761.

Zhao, Y., Zhao, Y., Shi, R., Wang, B., Waterhouse, G.I.N., Wu, L.Z., Tung, C.H., and Zhang, T. (2019). Tuning Oxygen Vacancies in ultrathin TiO_2 nanosheets to boost photocatalytic nitrogen fixation up to 700 nm. Adv. Mater. *31*, 1806482.

Zhou, L., Zhang, K., Hu, Z., Tao, Z., Mai, L., Kang, Y.M., Chou, S.L., and Chen, J. (2018a). Recent developments on and prospects for electrode materials with hierarchical structures for lithium-ion batteries. Adv. Energy Mater. *8*, 1701415.

Zhu, S., Li, L., Liu, J., Wang, H., Wang, T., Zhang, Y., Zhang, L., Ruoff, R.S., and Dong, F. (2018). Structural directed growth of ultrathin parallel birnessite on β-MnO_2 for high-performance asymmetric supercapacitors. ACS Nano *12*, 1033–1042.

Zou, Y., Zhang, W., Chen, N., Chen, S., Xu, W., Cai, R., Brown, C.L., Yang, D., and Yao, X. (2019). Generating oxygen vacancies in MnO hexagonal sheets for ultralong life lithium storage with high capacity. ACS Nano *13*, 2062–2071.

ISCI, Volume *23*

Supplemental Information

Oxygen Defects in β-MnO_2 Enabling High-Performance Rechargeable Aqueous Zinc/Manganese Dioxide Battery

Mingming Han, Jiwu Huang, Shuquan Liang, Lutong Shan, Xuesong Xie, Zhenyu Yi, Yiren Wang, Shan Guo, and Jiang Zhou

Supplemental Information

Table S1. A summary of the reported cathode materials for different Zn-ion battery system, related to Figure 4.

Cathode	Electrolyte	Capacity	Capacity retention	Reference
α-MnO_2	2M $ZnSO_4$ +0.1M $MnSO_4$	285 at 1/3 C	92% after 5000 cycles at 5 C	Pan et al., 2016
α-MnO_2	2M $ZnSO_4$+ 0.2M $MnSO_4$	301 at 100 mA g^{-1}	67% after 800 cycles at 7 A g^{-1}	Wu et al., 2018
δ-MnO_2	0.5M $Zn(TFSI)_2$	110 at 12.3 mA g^{-1}	48% after 125 cycles at 12.3 mA g^{-1}	Han et al., 2017
α-MnO_2	1M $ZnSO_4$	231 at 66 mA g^{-1}	45% after 75 cycles at 83 mA g^{-1}	Alfaruqi et al., 2016
α-MnO_2	1M $ZnSO_4$	233 at 83 mA g^{-1}	65% after 50 cycles at 83 mA g^{-1}	Alfaruqi et al., 2015a
σ-MnO_2	1M $ZnSO_4$ +0.2M $MnSO_4$	345 at 0.2 A g^{-1}	80% after 2000 cycles at 5 A g^{-1}.	Xiong et al., 2019
$Na_{0.44}Mn_2O_4 \cdot 1.5H_2O$	2M $ZnSO_4$ +0.2M $MnSO_4$	278 at 1 C	Nearly 100% after 2000 cycles at 8 C.	Wang et al., 2019
γ-MnO_2	1M $ZnSO_4$	285 at 0.05 mA cm^{-2}	37% after 40 cycles at 0.5 mA cm^{-2}	Alfaruqi et al., 2015b
β-MnO_2	1M $ZnSO_4$	270 at 100 mA g^{-1}	75% after 200 cycles at 0.2 A g^{-1}.	Islam et al., 2017
β-MnO_2	3M $Zn(CF_3SO_3)_2$+0.1M $Mn(CF_3SO_3)_2$	258 at 0.65C	94% after 2000 cycles at 6.5 C	Zhang et al., 2017
$NaV_3O_8 \cdot 1.5H_2O$	1M $ZnSO_4$+1M $NaSO_4$	380 at 50 mA g^{-1}	82% after 1000 cycles at 4 A g^{-1}	Wan et al., 2018
$Zn_{0.25}V_2O_5 \cdot nH_2O$	1M $ZnSO_4$	282 at 1 C	80% after 1000 cycles at 8 C	Kundu et al., 2016
$V_2O_5 \cdot nH_2O$	3M $Zn(CF_3SO_3)_2$	381 at 60 mA g^{-1}	71% after 900 cycles at 6 A g^{-1}	Yan et al., 2018
C-RZnHCF	3M $ZnSO_4$	69.1 at 60 mA g^{-1}	93% after 100 cycles at 300 mA g^{-1}	Zhang et al., 2015
β-MnO_2	3M $ZnSO_4$ +0.1M $MnSO_4$	302 at 50 mA g^{-1}	94% after 300 cycles at 500 mA g^{-1}	**This work**

Table S2. The R_s (the sum of electrolyte resistance and ohmic resistances of the cell components) and R_{ct} (charge-transfer) resistance values of D-β-MnO_2 and commercial β-MnO_2 at different cycles, related to Figure 4.

Sample		*Rct*	*Rs*
D-β-MnO_2	Initial	257	2.0
	5^{th} cycle	138	3.8
	10^{th} cycle	46	3.7
Commercial β-MnO_2	Initial	610	1.7
	5^{th} cycle	207	0.8
	10^{th} cycle	178	3.2

Table S3. The calculated bulk lattice parameters (Å) of β-MnO_2, compared with available experimental values. The calculated equilibrium lattice parameters are well consistent with the experimental data, related to Figure 1.

	This work	Other calculations (Wang et al., 2013)	Experimental (Bolzan et al., 1993)
a=b(Å)	4.4713	4.473	4.4041
c(Å)	2.9362	2.957	2.8765

Transparent Methods

Preparations of D-β-MnO_2 nanorods: In a typical experiment, 26 ml of $Mn(NO_3)_2$ solution (50% wt) was dissolved into distilled water (15 ml). Then, the mixed solution was ultrasoniced for 30 min and magnetically stirred for another 30 min at room temperature until a homogeneous pink solution was formed. Afterwards, the above solution was transferred into the autoclave (50 ml) and heated at 180 ℃ for 10 h, obtaining black β-MnO_2 powder. Then the obtained powder was calcinated in muffle furnace at air atmosphere at 450 ^{o}C for 1 hour, followed by $NaBH_4$ (0.25 M) reduction for 50 minutes. Finally, the D-β-MnO_2 powder was obtained.

Electrochemical tests: Firstly, the cathode electrodes were prepared by casting a slurry mixed with β-MnO_2 powder (70% wt), acetylene black (20% wt) and polyvinylidene fluoride (10% wt) onto the stainless steel wire mesh (SSWM, 400 orders) with the area of 1.13 cm^2. Then they were dried at 80 ℃ for 12 h in a vacuum atmosphere. The electrochemical performances of the MnO_2 electrodes were tested by assembling with the Zn foil anode (the purity greater than or equal to 99.9%, without using a reference electrode), glass fiber separator and 3 M $ZnSO_4$ electrolyte with 0.1 M $MnSO_4$ additives the CR2016 coin-type cells. Cyclic voltammetry measurements were conducted on an electrochemical workstation (CHI660E, CHI Instruments) between 0.8-1.8 V. Galvanostatic charge/discharge and cycling performance were carried on the LAND-2001A battery-testing system.

Material Characterizations: The morphology of MnO_2 powder was characterized on FEI Nova NanoSEM 230. The crystal phase was analysed through a X-ray powder diffraction mechanism (Rigaku D/Max-2500, Cu Kα radiation, λ = 1.54178 Å). The FTIR were tested on a BIORAD FTS 6000 FTIR. TEM, HR-TEM images, SAED patterns and EDX mappings were collected on Titan G2 60-300 machine. XPS were carried out on an ESCALAB 250Xi X-ray photoelectron spectrometer (Thermo Fisher) to identify the surface chemical composition and investigate the evolution of Mn valence.

Computation Details

All the calculations were carried out in the Vienna ab initio simulation package (VASP) (Kresse et al., 1996) with generalized gradient approximation (GGA) functional of Perdew, Burke, and Ernzerhof (PBE) (Perdew et al., 1996) combined with projector augmented wave (PAW) (Kresse et al., 1999). PBE+U approaches are applied to describe the d states of Mn compound. The Hubbard U value of Mn atoms is taken as 4 eV based on our calculations and literatures. For bulk lattice optimizations, a cutoff energy of 500 eV and a Monk-horst pack k-point mesh 5*5*7 was adopted. The total energy convergence was set to less than 10^{-5} eV and the force on each atom was less than 0.02 eV/Å in both structural optimizations and the self-consistent calculations. All atom coordinates and lattice vectors are fully relaxed for each structure. A 2*2*2 β-MnO_2 supercell is applied with 16 Mn atoms and 32 O atoms. Spin-polarizations are included in all the calculations, and antiferromagnetic ordering is considered for β-MnO_2.

Formation energies (E_f) for the defects are considered as

$$E_f = E_{\mathrm{II}} - E_{\mathrm{I}} - \sum N_i \cdot \mu_i + qe_{\mathrm{VBM}}$$

Here, E_{II} and E_I stand for the total energy of the supercell with or without concerned defects. N_i stands for the numbers of atoms of type i that have been added to ($N_i > 0$) or removed from ($N_i < 0$) the supercell when defect is created, and μ_i represents the relevant chemical potentials of these atoms. q is the valence state for the induced defect, and e_{VBM} is the VBM of the host supercell. The chemical potential of O is taken as the energy of oxygen which refers to the O-rich condition, Zn and H are taken as the relevant bulk energy.

The reaction equation of the Zn/D-*β*-MnO_2 battery, related to Figure 5.

The positive electrode:

$$H_2O \leftrightarrow H^+ + OH^-$$
$$MnO_2 + H^+ + e- \leftrightarrow MnOOH$$
$$1/2\ Zn^{2+} + OH^- + 1/6\ ZnSO_4 + x/6\ H_2O \leftrightarrow 1/6\ ZnSO_4[\ Zn(OH_2)]_3\ xH_2O$$

The negative electrode:

$$1/2\ Zn \leftrightarrow 1/2\ Zn^{2+} + e-$$

Overall:

$$MnO_2 + 1/2\ Zn + x/6\ H_2O + 1/6\ ZnSO_4 \leftrightarrow MnOOH + 1/6\ ZnSO_4[Zn(OH)_2]_3\ xH_2O$$

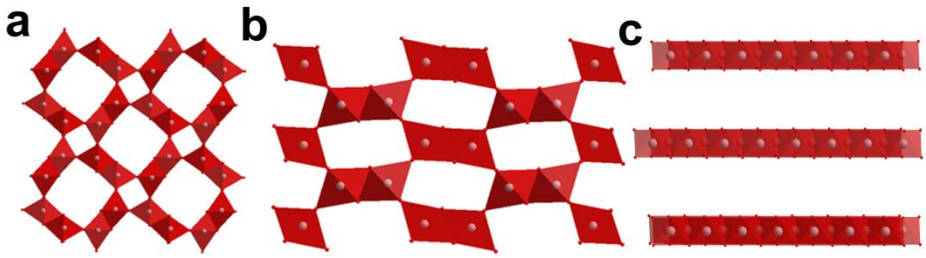

Figure S1. a-c) Crystal structures of α-MnO_2, γ-MnO_2 and δ-MnO_2, related to Figure 2.

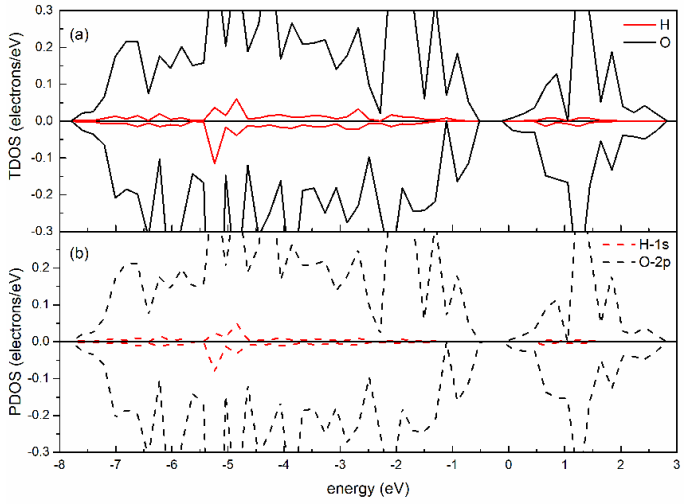

Figure S2. The calculated (a) TDOS and (b) PDOS of inserted H^+ and the NN-O in MnO_2 supercell with a (V_O+ H^+) as shown in Fig.1(f) , related to Figure 1.

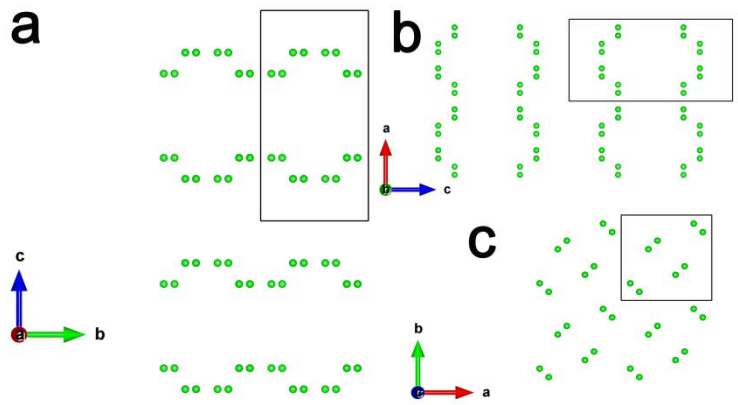

Figure S3. a) The front view, b) the side view, c) the top view of the apace group of P42/mnm, related to Figure 2.

The complete international symbol of P42/mnm is $P\frac{4_1}{m}\frac{2_1}{n}\frac{2}{m}$, where P represents simple grid, 4_1 represents that "c" axis is the 4_1 rotation axis, the first m represents that the plane vertical to the c axis is specular plane, 2_1 represents that the direction of "a"axis is the 2_1 rotation axis, n represents that the plane vertical to the"a"axis is diagonal slip plane and the slip direction is $\frac{a+b}{2}$, the "2" represents that the diagonal line of $\frac{a+b}{2}$ is the secondary axis, the second "m" represents the plane vertical to the diagonal line of $\frac{a+b}{2}$ is a specular plane.

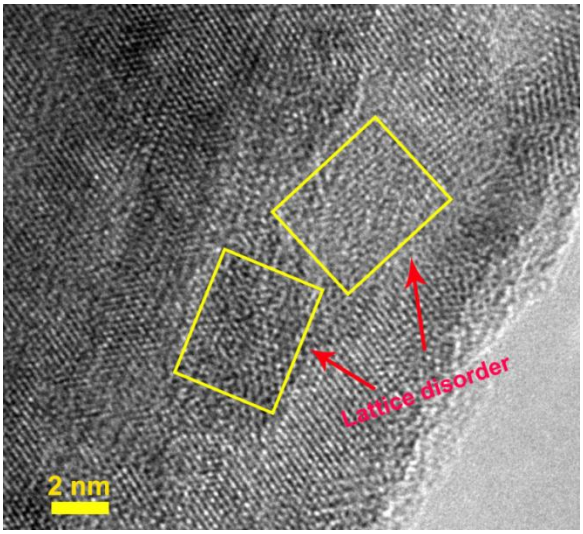

Figure S4. HR-TEM image of D-β-MnO_2, related to Figure 3.

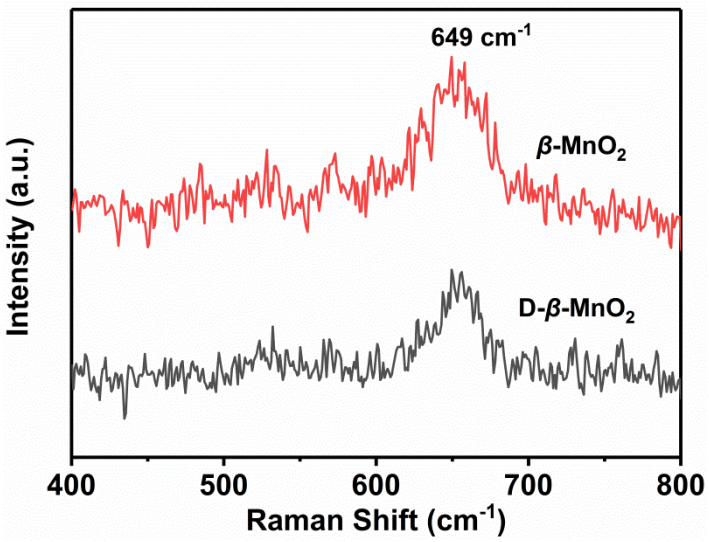

Figure S5. Raman spectra of D-β-MnO_2 and commercial β-MnO_2, related to Figure 3.

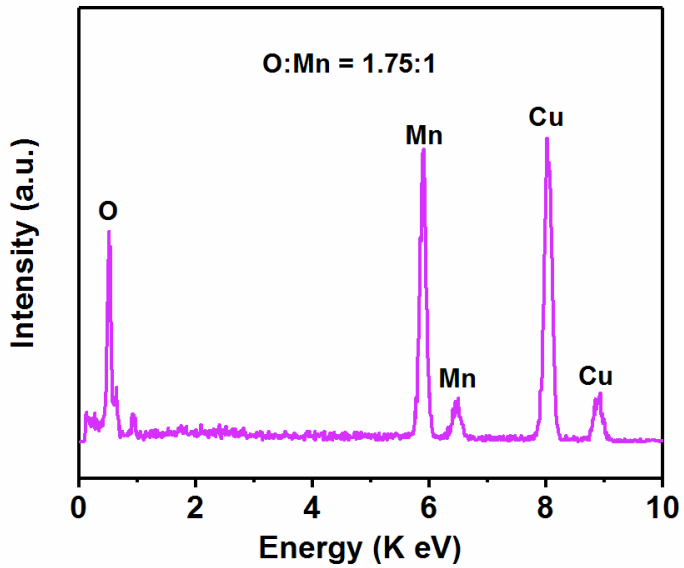

Figure S6. EDX of the D-β-MnO_2 sample, related to Figure 3.

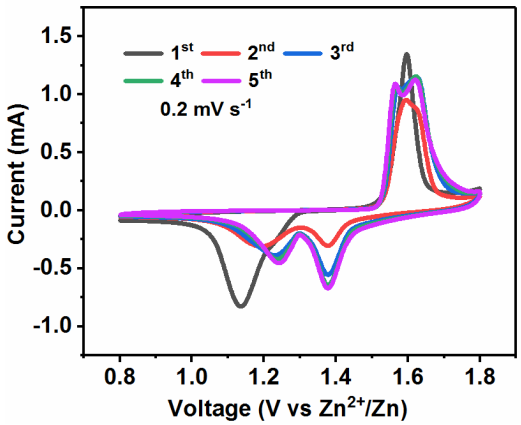

Figure S7. CV curves of the initial 5 cycles at 0.2 mV s^{-1} of the D-β-MnO_2 electrode, related to Figure 4.

The cathodic peaks centered at about 1.25 and 1.40 V were attributed to the insertion of H^+ into the β-MnO_2 host (H^+ is the main charge carrier in this work), and the anodic peaks centered at 1.56 V with a shoulder at 1.61 V correspond to the extraction of H^+ from β-MnO_2 cathode, accompanying the evolution between Mn(IV) and Mn(III)/Mn(II) states.

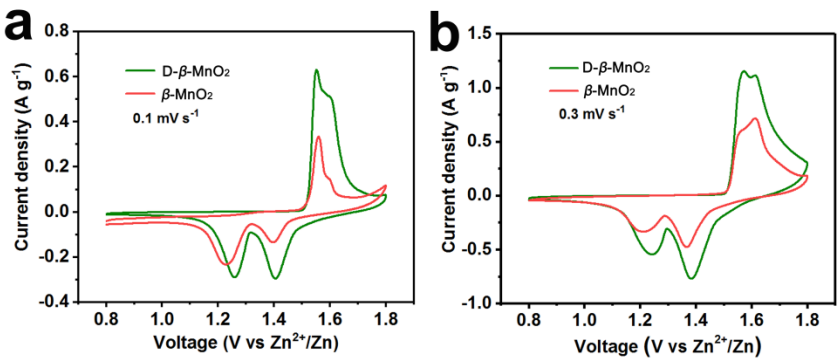

Figure S8. CV curves at 0.1 and 0.3 mV s^{-1} of the D-β-MnO_2 and commercial β-MnO_2, related to Figure 4.

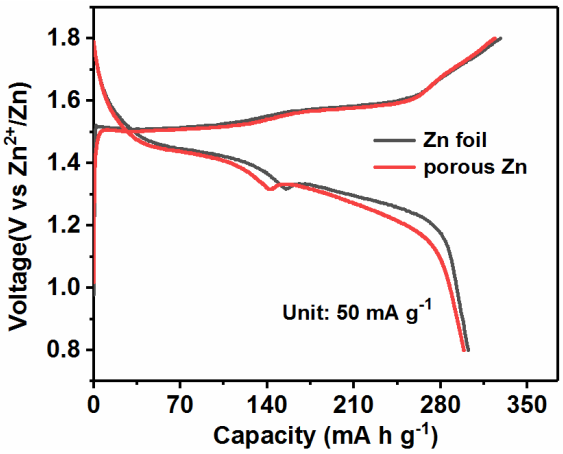

Figure S9. GCD profiles of the Zn/D-β-MnO_2 cell using the porous Zn and Zn foil anode, related to Figure 4.

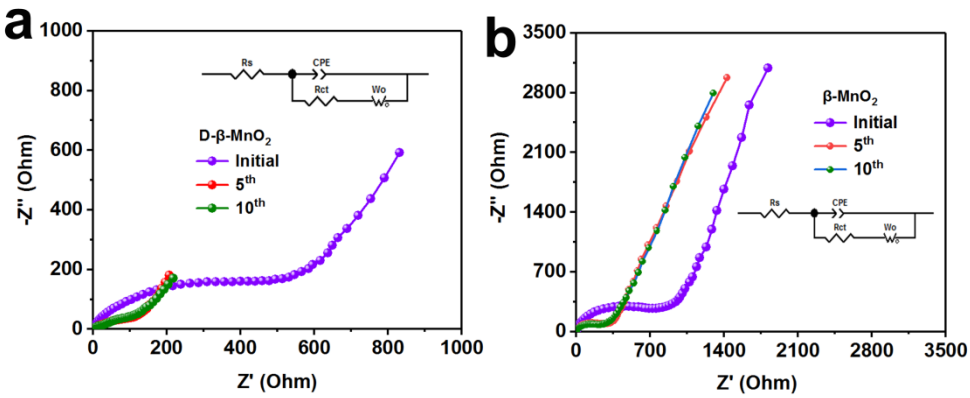

Figure S10. The electrochemical impedance spectra of D-β-MnO_2 and commercial β-MnO_2 electrodes at different cycles, related to Figure 4.

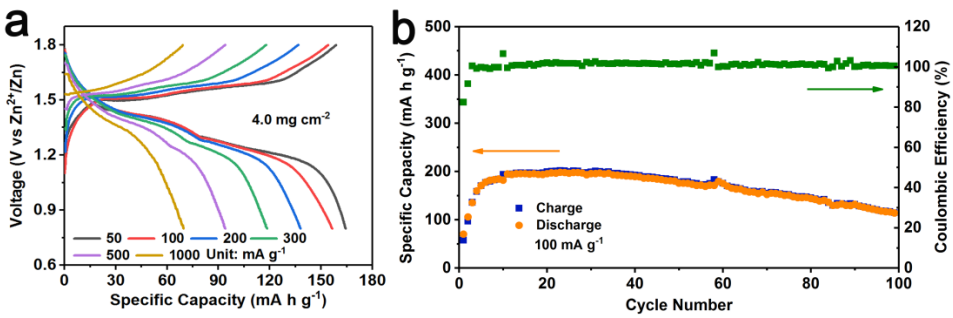

Figure S11. Electrochemical performances of the Zn/D-β-MnO_2 batteries with a high mass loading of 4.0 mg cm^{-2}. a,) Rate capacities; b) Cycling performances at 100 mA g^{-1}, related to Figure 4.

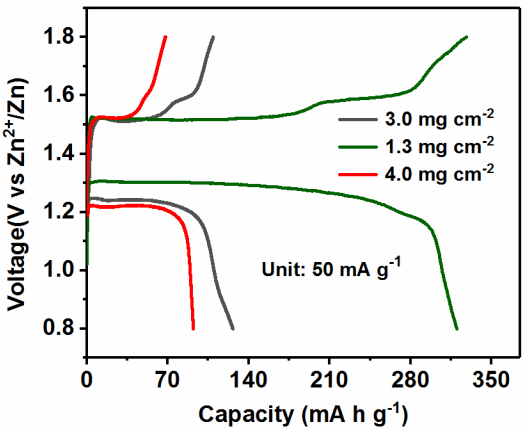

Figure S12. The GCD curves in the initial cycle of D-β-MnO_2 electrode with different mass loadings, related to Figure 4.

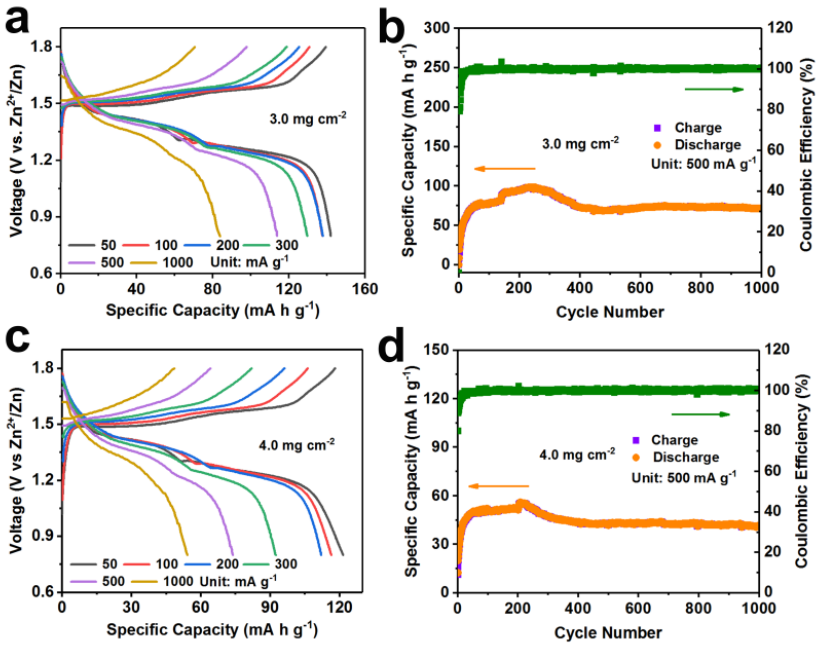

Figure S13. Electrochemical performances of the commercial β-MnO_2 electrodes with high mass loadings of 3.0 and 4.0 mg cm^{-2}. a, c) Rate capacities; b, d) Cycling performances at 500 mA g^{-1}, related to Figure 4.

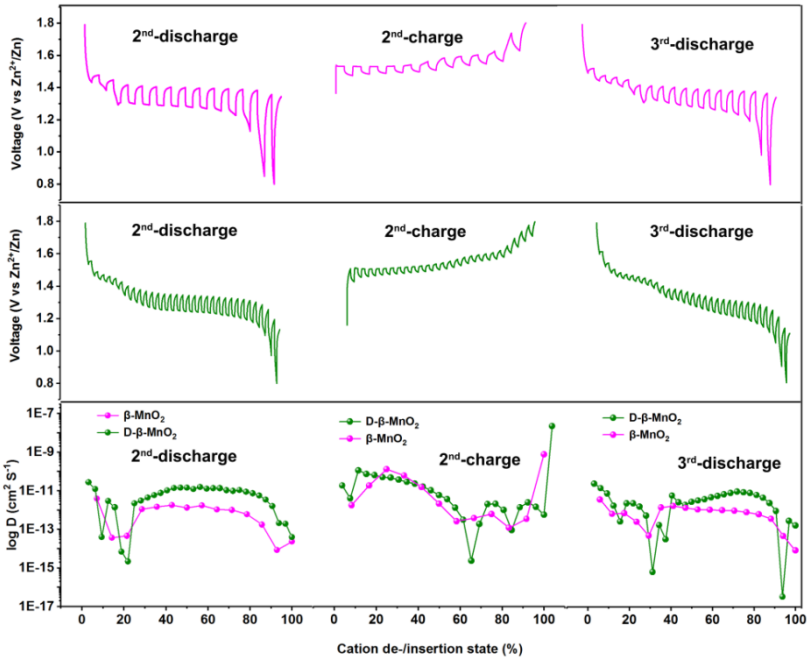

Figure S14. GITT curves and the corresponding diffusion coefficients at different states of the H^+ in D-β-MnO_2 and commercial β-MnO_2 electrodes, related to Figure 4.

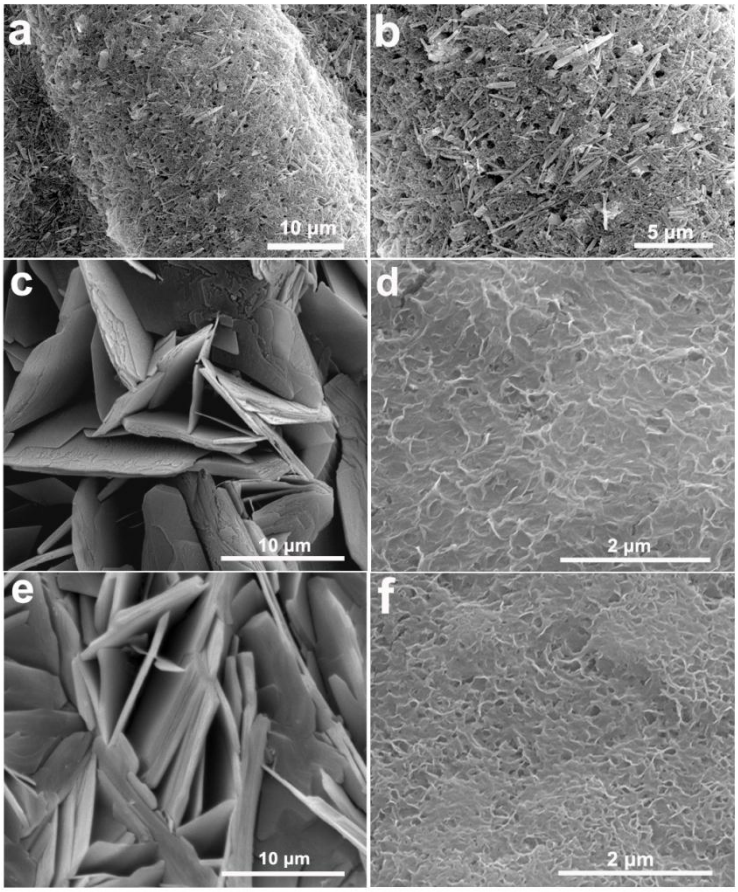

Figure S15. The *ex-situ* SEM images of D-β-MnO_2 electrode. a, b) Initial state; c, e) 1st, 2nd fully discharged state; d, f) 1st, 2nd fully charged state, related to Figure 5.

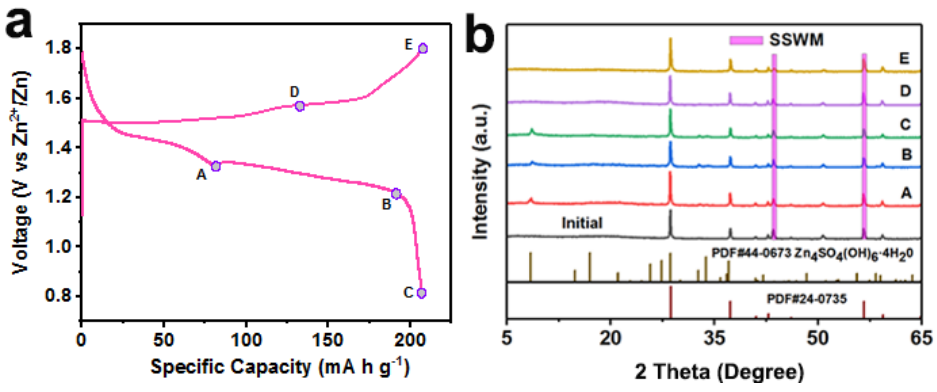

Figure S16. a) GCD curves at 50 mA g^{-1} for the second cycle; b) The corresponding *ex-situ* XRD patterns at selected states of commercial β-MnO_2 electrode, related to Figure 5.

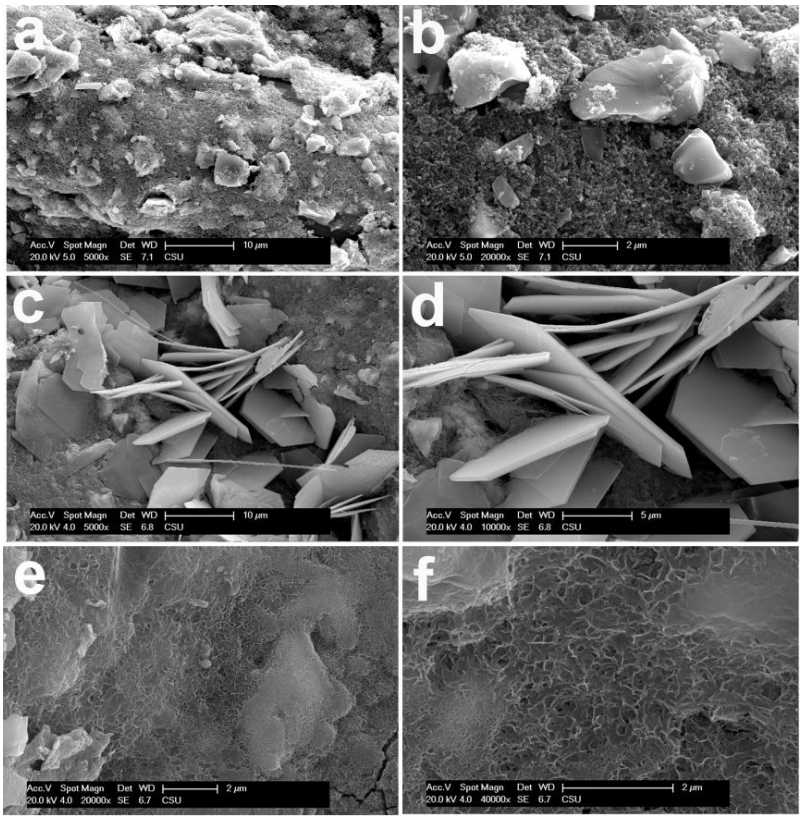

Figure S17. The *ex-situ* SEM images of commercial β-MnO_2 electrode. a, b) Initial state; c, d) Fully discharged state and e, f) fully charged state at the second cycle, related to Figure 5.

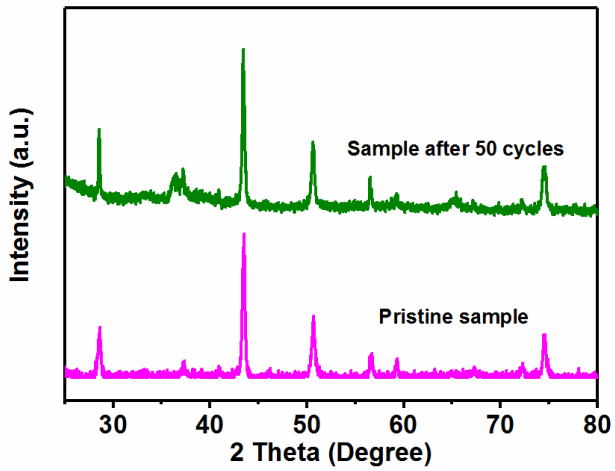

Figure S18. XRD patterns of the D-β-MnO_2 electrode at the initial and after 50 cycles state, related to Figure 5.

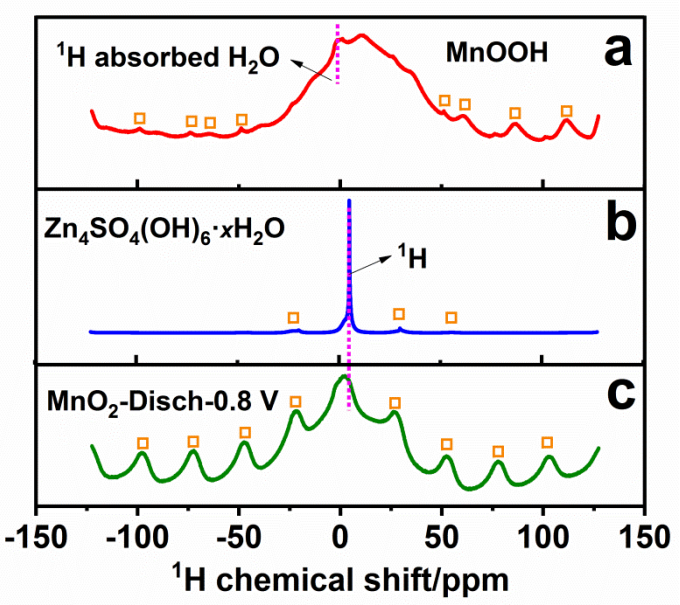

Figure S19. The solid state ^{1}H NMR spectra. a), MnOOH; b) $Zn_4SO_4(OH)_6$ xH_2O and c) MnO_2 electrode discharged to 0.8V, related to Figure 6.

The solid state ^{1}H NMR spectra were carried out to further confirm the reaction mechanism. The peaks marked by the little square frame are spinning side bands in NMR spectrum. Two isotropic peaks centered at 10.3 and -1.6 ppm in Figure S19a are attributed to the resonance from MnOOH and the physical absorbed H_2O on the surface of MnOOH. (Pan et al., 2016) Figure S19b shows a sharp ^{1}H signal at 5.3 ppm, which is resonated from the numberous hydroxyl groups and crystalliferous water in $Zn_4SO_4(OH)_6$ xH_2O compound. (Paik et al., 2001) Remarkably, the D-β-MnO_2 electrode at discharged state (Figure S19c) shows a dominant peak at 2.1 ppm resonated from $Zn_4SO_4(OH)_6$ xH_2O. The slight up shift is due to the difference of magnetic susceptibility between a composite electrode and $Zn_4SO_4(OH)_6$ xH_2O compound, (Pan et al., 2016) which may be caused by the insertion of H^+. Additionally, the missing peak at 10 ppm from MnOOH is probably because the composite electrode is coated by quantities of $Zn_4SO_4(OH)_6$ xH_2O, which limited the signal of MnOOH inside the composite electrode.

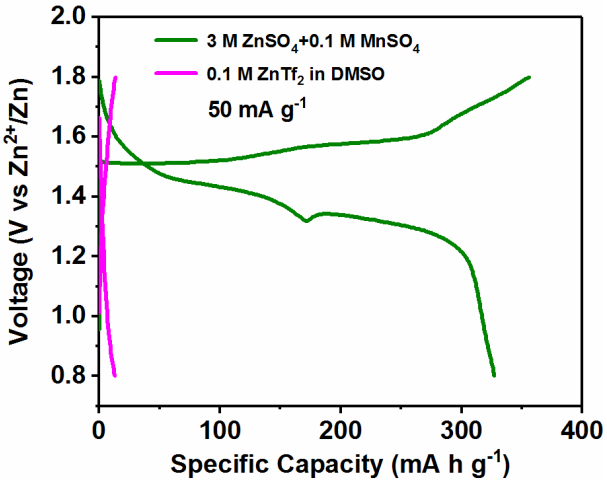

Figure S20. The comparison of discharge capacities of D-β-MnO_2 electrodes in organic (0.1 M $Zn(Tf)_2$/DMSO) and aqueous electrolyte (2^{nd} cycle, current density of 0.05 A g^{-1}), related to Figure 5.

References

Pan, H., Shao. Y., Yan, P., Cheng, Y., Han, K. S., Nie, Z., Wang, C., Yang, J., Li, X., Bhattacharya, P., Mueller K. T., Liu, J. (2016). Reversible aqueous zinc/manganese oxide energy storage from conversion reactions. Nat. Energy, *1*, 16039.

Wu B, Zhang G, Yan M, Xiong, T., He, P., He, L., Xu, X., Mai, L. (2018). Graphene scroll coated α-MnO_2 nanowires as high-performance cathode materials for aqueous Zn-ion battery. Small, *14*, 1703850.

Han, S. D., Kim, S., Li, D., Petkov, V., Yoo, H. D., Phillips, P. J., Wang, H., Kim, J. J., More, K. L., Key, S., Klie, R. F., Cabana, J., Stamenkovic, V. R., Fister, T. T., Markovic, N. M., Burrell, A. K., Tepavcevic, S., Vaughev, J. T. (2017). Mechanism of Zn insertion into nanostructured *δ*-MnO_2: a nonaqueous rechargeable Zn metal battery. Chem. Mater. *29*, 4874-4884.

Alfaruqi, M. H., Islam, S., Gim, J., Song, J., Kim, S., Pham, D. T., Jo, J., Xiu, Z., Mathew, V., Kim, J. (2016). A high surface area tunnel-type *α*-MnO_2 nanorod cathode by a simple solvent-free synthesis for rechargeable aqueous zinc-ion batteries. Chem. Phys. Lett. *650*, 64-68.

Alfaruqi, M. H., Gim, J., Kim, S., Song, J., Jo, J., Kim, S., Mathew, V., Kim, J. (2015a). Enhanced reversible divalent zinc storage in a structurally stable α-MnO_2 nanorod electrode. J. Power Sources, 2015, *288*, 320-327.

Xiong, T., Yu, Z. G., Wu, H., Du, Y., Xie, Q., Chen, J., Zhang, Y. W., Pennycook, S. J., Lee, W. S. V., Xue, J. (2019). Defect engineering of oxygen-deficient manganese oxide to achieve high-performing aqueous zinc ion battery. Adv. Energy Mater. *9*, 1803815.

Wang, D., Wang, L., Liang, G., Li, H., Liu, Z., Tang, Z., Liang, J., Zhi, C. (2019). A superior δ-MnO_2 cathode and a self-healing Zn-δ-MnO_2 battery. ACS Nano, *13*, 10645-10652.

Alfaruqi, M. H., Mathew, V., Gim, J., Kim, S., Song, J., Baboo, J. P., Choi, S. H., Kim, J. (2015b). Electrochemically induced structural transformation in a γ-MnO_2 cathode of a high capacity zinc-ion battery system. Chem. Mater. *27*, 3609-3620.

Islam, S., Alfaruqi, M. H., Mathew, V., Song, J., Kim, S., Kim, S., Jo, J., Baboo, J. P., Pham, D. T., Putro, D. Y., Sun, Y. K., Kim, J. (2017). Facile synthesis and the exploration of the zinc storage mechanism of β-MnO_2 nanorods with exposed (101) planes as a novel cathode material for high performance eco-friendly zinc-ion batteries. J. Mater. Chem. A, *5*, 23299-23309.

Zhang, N., Cheng, F., Liu, J., Wang, L., Long, X., Liu, X., Li, F., Chen, J. (2017). Rechargeable aqueous zinc-manganese dioxide batteries with high energy and power

densities. Nat. Commun. *8*, 405-413.

Wan, F., Zhang, L., Dai, X., Wang, X., Niu, Z., Chen, J. (2018). Aqueous rechargeable zinc/sodium vanadate batteries with enhanced performance from simultaneous insertion of dual carriers. Nat. Commun. *9*, 1656-1666.

Kundu D, Adams B D, Duffort V, Vajargah, S. H., Nazar, L. N. (2016). A high-capacity and long-life aqueous rechargeable zinc battery using a metal oxide intercalation cathode. Nat. Energy, 1, 16119.

Yan, M., He, P., Chen, Y., Wang, S., Wei, Q., Zhao, K., Xu, X., An, Q., Shuang, Y., Shao, Y., Mueller, K. T., Mai, L., Liu, J., Yang, J. (2018). Water-lubricated intercalation in V_2O_5 nH_2O for high-capacity and high-rate aqueous rechargeable zinc batteries. Adv. Mater. *30*, 1703725.

Zhang, L., Chen, L., Zhou, X., Liu, Z. (2015). Morphology-dependent electrochemical performance of zinc hexacyanoferrate cathode for zinc-ion battery. Sci. Rep. *5*, 18263.

Wang, D., Liu, L. M., Zhao, S. J., Li, B. H., Liu, H., Lang, X. F. (2013). β-MnO_2 as a cathode material for lithium ion batteries from first principles calculations. Phys. Chem. Chem. Phys. *15*, 9075-9083.

Bolzan, A. A., Fong, C., Kennedy, B. J., Howard, C. J. (1993). Powder neutron diffraction study of pyrolusite β-MnO_2. Aus. J. Chem. *46*, 939-944.

Kresse, G., Furthmüller, J. (1996). Efficient iterative schemes for ab initio total-energy calculations using a plane-wave basis set. Phys. Rev. B, *54*, 169-186.

Perdew, J. P., Burke, K., Ernzerhof, M. (1996). Generalized gradient approximation made simple. Phys. Rev. lett. *77*, 3865-3868.

Kresse, G., Joubert, D. (1999). From ultrasoft pseudopotentials to the projector augmented-wave method. Phys. Rev. B, *59*, 1758-1775.

Paik, Y., Osegovic J. P., Wang, F., Bowden, W., Grey, C. P. (2001). ^{2}H MAS NMR studies of the manganese dioxide tunnel structures and hydroxides used as cathode materials in primary batteries. J. Am. Chem. Soc. *123*, 9367.